

# On the formation of H $\alpha$ line emission around classical T Tauri stars

Ryuichi Kurosawa<sup>1\*</sup>, Tim J. Harries<sup>1</sup> and Neil H. Symington<sup>2</sup>

<sup>1</sup>School of Physics, University of Exeter, Stocker Road, Exeter EX4 4QL.

<sup>2</sup>School of Physics and Astronomy, University of St. Andrews, North Haugh, St. Andrews, Fife, KY16 9SS.

Dates to be inserted

## ABSTRACT

We present radiative transfer models of the circumstellar environment of classical T Tauri stars, concentrating on the formation of the H $\alpha$  emission. The wide variety of line profiles seen in observations are indicative of both inflow and outflow, and we therefore employ a circumstellar structure that includes both magnetospheric accretion and a disc wind. We perform systematic investigations of the model parameters for the wind and the magnetosphere to search for possible geometrical and physical conditions which lead to the types of profiles seen in observations. We find that the hybrid models can reproduce the wide range profile types seen in observations, and that the most common profile types observed occupy a large volume of parameter space. Conversely, the most infrequently observed profile morphologies require a very specific set of models parameters. We investigate the wind contribution to the line profile as a function of model parameters, and examine the reliability of H $\alpha$  as a mass accretion diagnostic. Finally, we examine the H $\alpha$  spectroscopic classification used by Reipurth et. al, and discuss the basic physical conditions that are required to reproduce the profiles in each classified type.

**Key words:** stars: formation – circumstellar matter – radiative transfer – stars: pre-main-sequence

## 1 INTRODUCTION

T Tauri stars (TTS) are young ( $\gtrsim 3 \times 10^6$  yrs, Appenzeller & Mundt 1989) low-mass objects, and are the progenitors of solar-type stars. Classical T Tauri stars (CTTS) exhibit strong H $\alpha$  emission, and typically have spectral types of F–K. Some of the most active CTTS show emission in higher Balmer lines and metal lines (e.g., Ca II H and K). They also exhibit excess continuum flux in the ultraviolet (UV) and infrared (IR). Their spectral energy distribution and polarisation data suggest the presence of circumstellar discs, which plays an important role in regulating dynamics of gas flows around CTTS (e.g. Camenzind 1990).

Many observational studies (e.g., Herbig 1962; Edwards et al. 1994; Kenyon et al. 1994; Reipurth, Pedrosa, & Lago 1996; Alencar & Basri 2000) of CTTS line profiles have revealed evidence for both outward wind flows and inward accretion flows, characterised by the blue-shifted absorption features in H $\alpha$  profiles and the redshifted inverse P Cygni (IPC) profiles respectively. Typical mass-loss rates of CTTS are about  $10^{-9} M_{\odot} \text{ yr}^{-1}$  to  $10^{-7} M_{\odot} \text{ yr}^{-1}$  (e.g., Kuhu 1964; Edwards et al. 1987; Hartigan, Edwards, & Ghandour 1995), and the mass-accretion rates are also about  $10^{-9} M_{\odot} \text{ yr}^{-1}$  to  $10^{-7} M_{\odot} \text{ yr}^{-1}$  (e.g., Kenyon & Hartmann 1987; Bertout, Basri, & Bouvier 1988; Gullbring et al. 1998). Recent H $\alpha$  spectro-astrometric observations by Takami, Bailey,

& Chrysostomou (2003) provide indirect evidence for the presence of bipolar and monopolar outflows down to  $\sim 1$  au scale (e.g. CS Cha and RU Lup). Similarly, ESO VLT observations using high-resolution ( $R = 50\,000$ ) two-dimensional spectra of edge-on CTTS (HH30\*, HK Tau B, and HV Tau C) by Appenzeller et al. (2005) show extended H $\alpha$  emission in the direction perpendicular to the obscuring circumstellar disc, suggesting the presence of the bipolar outflows. On an even larger scale, *HST* observations of HH30 (Burrows et al. 1996) trace the jet to within  $\lesssim 30$  au of the star. The jet has a cone shape with an opening angle of  $3^\circ$  between 70 and 700 au (Königl & Pudritz 2000). Alencar & Basri (2000) found about 80 per cent of their sample (30 CTTS) show blue-shifted absorption components in at least one of the Balmer lines and Ca K.

In the currently favoured model of accretion in CTTS, the accretion disc is disrupted by the magnetosphere, which channels the gas from the disc onto the stellar surface (e.g., Uchida & Shibata 1985; Königl 1991; Collier Cameron & Campbell 1993; Shu et al. 1994). This picture is supported by recent measurements of strong ( $\sim 10^3$  G) magnetic fields in CTTS (e.g., Johns-Krull et al. 1999; Symington et al. 2005b) and by radiative transfer models which reproduce the gross characteristics of observed profiles for some TTS (Muzerolle, Calvet, & Hartmann 2001). In particular the magnetospheric accretion (MA) model explains blue-ward asymmetric emission line profiles as resulting from the partial occultation of the flow by the stellar photosphere, while inverse P Cygni profiles

\* E-mail:rk@astro.ex.ac.uk

in the MA model result from inflowing material at near free-fall velocities seen projected against hotspots on the stellar surface.

Despite these successes, the overwhelming observational evidence for outflow in the CTTS suggests that the MA model is only one component of a complex circumstellar environment. Clearly, one must include the contribution of any wind/jet flow if one wishes to both accurately predict the mass-accretion rate and also determined the mass-loss rate of CTTS via emission profile modelling. The first attempt in this direction was made by Alencar et al. (2005) who demonstrated that the observed H $\alpha$ , H $\beta$  and Na D lines of RW Aur are better reproduced by the radiative transfer model which included a collimated disc-wind arising from near the inner edge of the accretion disc.

The main aim of this paper is to find a simple kinematic model which can reproduce the wide variety of the observed profiles, and to perform empirical studies of line formation in an attempt to place morphological classification schemes on a firmer physical footing. We will also discuss whether our model is consistent with some predictions made by recent (magneto-hydrodynamics) MHD studies i.e.  $\mu = \dot{M}_{\text{wind}}/\dot{M}_{\text{acc}} \approx 0.1$  (e.g. Königl & Pudritz 2000).

In section 2, the model assumptions, and the basic model configurations are presented. We discuss the radiative transfer model used to compute the profiles in section 3, and the results of model calculations are given in section 4. We discuss our results in the context of Reipurth's classification scheme in section 5, and our summary and conclusions are presented in section 6.

## 2 MODEL CONFIGURATION

In order to understand how the different parts of the CTTS circumstellar environment contribute to the formation of H $\alpha$ , the model space is divided into four different regions: (1) a central continuum source, (2) the magnetospheric accretion flow, (3) the wind outflow, and (4) the accretion disc. Fig. 1 depicts the relative location of the regions in the model space. The density is assumed to be rotationally symmetric around the  $z$ -axis. The innermost radius of the magnetosphere at the equatorial plane coincides with the inner radius of the accretion disc. From the innermost part of the accretion disc, the gas falls freely, moving along the magnetic field onto the surface of the star. In the following subsections we describe the details of model components.

### 2.1 The continuum source

We adopt stellar parameters of a typical classical T Tauri star for the central continuum source, i.e. radius ( $R_*$ ), mass ( $M_*$ ), and effective temperature the photosphere ( $T_{\text{ph}}$ ) are  $2 R_\odot$ ,  $0.5 M_\odot$ , and 4000 K respectively. The model atmosphere of Kurucz (1979) with  $T_{\text{ph}} = 4000$  K and  $\log g_* = 3.5$  (cgs) defines the photospheric contribution to the continuum flux. The parameters are summarised in Table 1.

An additional continuum source is considered for models which includes magnetospheric accretion: as the infalling gas approaches the stellar surface, it decelerates in a strong shock, and is heated to  $\sim 10^6$  K. The X-ray radiation produced in the shock will be absorbed by the gas locally, and re-emitted in optical and UV radiation (Königl 1991; Hartmann, Hewett, & Calvet 1994). This will create hot rings where the magnetic field intersects with the surface. We assume that the free-falling kinetic energy is thermalized in the radiating layer, and is re-emitted as blackbody radiation with a single temperature. With the parameters of the magnetosphere and the

star given above (Table 1), about 8 per cent of the surface is covered by the hot rings. If the mass-accretion rate is  $10^{-7} M_\odot \text{ yr}^{-1}$ , the ratio of this accretion luminosity to the photospheric luminosity is about 0.5, and the corresponding temperature of the hot rings is about 6400 K. The continuum emission from the hot rings is taken into account when computing the line profiles.

### 2.2 The magnetosphere

We adopt the MA flow model of Hartmann et al. (1994), as done by Muzerolle et al. (2001) and by Symington, Harries, & Kurosawa (2005a), in which the gas accretion on to the stellar surface from the innermost part of the accretion disc occurs through a dipolar stellar magnetic field. The magnetic field is assumed to be so strong that the gas flow does not affect the underlying magnetic field itself. As shown in Fig. 1 (region 2), the innermost radius ( $R_{\text{mi}}$ ) of the magnetosphere at the equatorial plane ( $z = 0$ ) is assigned to be same as the inner radius ( $R_{\text{di}}$ ) of the accretion disc where the flow is truncated. In our models,  $R_{\text{mi}}$  and the outer radius ( $R_{\text{mo}}$ ) of the magnetosphere (at the equatorial plane) are set to be  $2.2 R_\odot$  and  $3.0 R_\odot$  respectively. The geometry of the magnetic field/stream lines is fixed for all calculations. We note that this magnetospheric geometry is identical to the “small/wide” model of Muzerolle et al. (2001).

The magnetic field and the gas stream lines are assumed to have the following simple form:

$$r = R_m \sin^2 \theta \quad (1)$$

(see Ghosh, Pethick, & Lamb 1977) where  $r$ , and  $\theta$  are the radial and the polar component of a field point position vector in the accretion stream.  $R_m$  is the radial distance to the field line at the equatorial plane ( $\theta = \pi/2$ ), and its value is restricted between  $R_{\text{mi}}$  and  $R_{\text{mo}}$  (Figure 1). Using the field geometry above and conservation of energy, the velocity and the density of the accreting gas along the steam line are found as in Hartmann et al. (1994).

The temperature structure of the magnetospheric used by Hartmann et al. (1994) is adopted here. They computed the temperature, assuming a volumetric heating rate which is proportional to  $r^{-3}$ , by solving the energy balance of the radiative cooling rate of Hartmann et al. (1982) and the heating rate (Hartmann et al. 1994). Martin (1996) presented a self-consistent determination of the thermal structure of the inflowing gas along the dipole magnetic field (equation 1) by solving the heat equation coupled to the rate equations for hydrogen. He found that main heat source is adiabatic compression due to the converging nature of the flow, and the major contributors to the cooling process are bremsstrahlung radiation and line emission from Ca II and Mg II ions. The results of Martin (1996) qualitatively agree with that of Hartmann et al. (1994).

### 2.3 The disc wind

The magneto-centrifugal wind paradigm, first proposed by Blandford & Payne (1982), has been often used to model the large-scale wind structure of T Tauri stars, or the observed optical jets (e.g. HH 30 jet by Burrows et al. 1996; Ray et al. 1996). The launching of the wind from a Keplerian disc is typically done by treating the equatorial plane of the disc as a mass-injecting boundary condition (e.g., Shu et al. 1994; Ustyugova et al. 1995; Ouyed & Pudritz 1997; Krasnopolksy et al. 2003). Depending on the location of the open magnetic fields anchored to the disc, two different types of winds are produced. If the field is constrained to be near

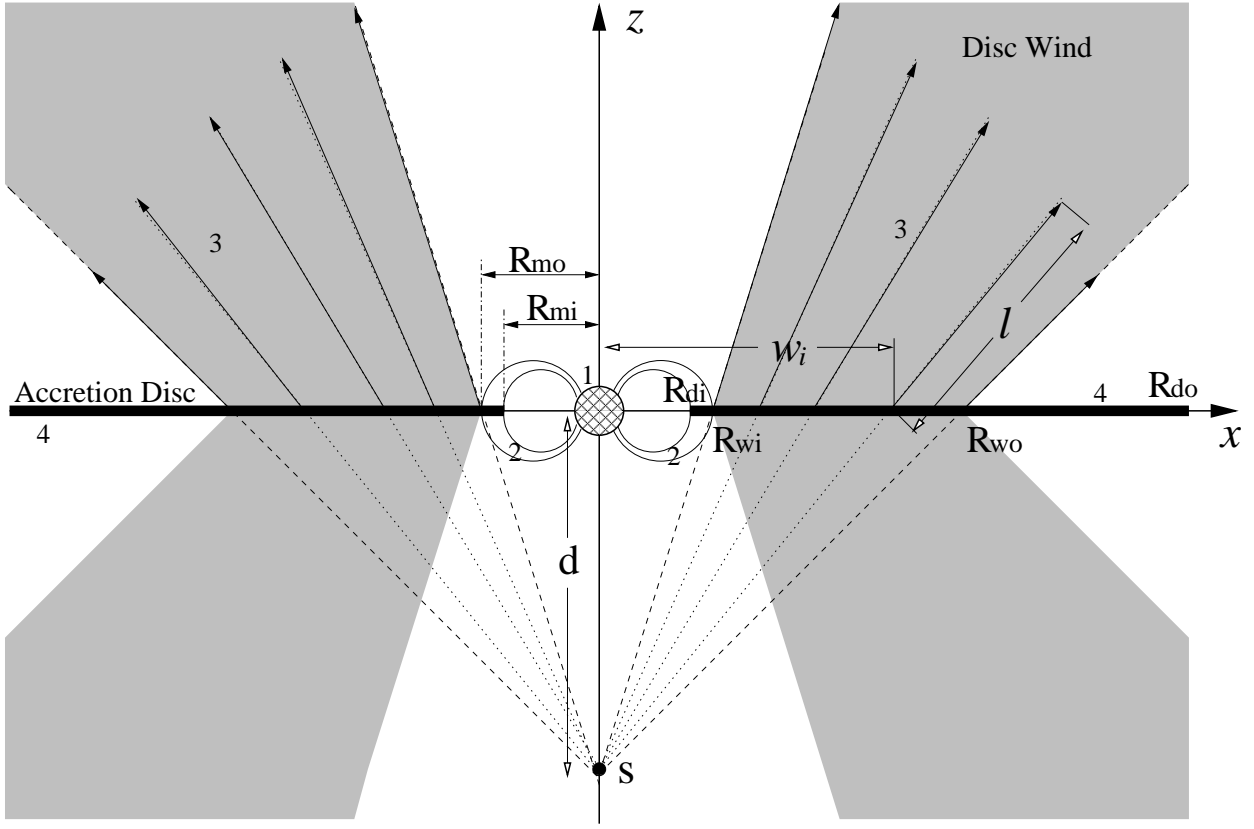


**Figure 1.** Basic model configuration of the disc-wind-magnetosphere hybrid model. The system consist of four components: (1) the continuum source located at the origin ( $o$ ) of the cartesian coordinates ( $x, y, z$ ) – the  $y$ -axis is into the paper, (2) the magnetospheric accretion flow, (3) the disc wind, and (4) the accretion disc. The disc wind originates from the disc surface between  $w_i = R_{wi}$  and  $w_o = R_{wo}$  where  $w_i$  is the distance from the  $z$  axis on the equatorial plane. The wind source points ( $S$ ), from which the stream lines diverges, are placed at distance  $d$  above and below the star. The degree of wind collimation is controlled by changing the value of  $d$ .

**Table 1.** Summary of the reference classical T Tauri star model parameters.

Parameters	$R_*$ [ $R_\odot$ ]	$M_*$ [ $M_\odot$ ]	$T_{\text{ph}}$ [K]	$R_{\text{mi}}$ [ $R_*$ ]	$R_{\text{mo}}$ [ $R_*$ ]	$\dot{M}_{\text{acc}}$ [ $M_\odot \text{ yr}^{-1}$ ]	$\dot{M}_{\text{wind}}$ [ $M_\odot \text{ yr}^{-1}$ ]	$R_{\text{di}}$ [ $R_*$ ]	$R_{\text{do}}$ [au]
	2.0	0.5	4000	2.2	3.0	$10^{-7}$	$10^{-8}$	2.2	100

the co-rotation radius of stellar magnetosphere, an “X-wind” (Shu et al. 1994) is produced. If the open field lines are located in a wider area of the disc, a “disc-wind” similar to that of Königl & Pudritz (2000) is produced (Krasnopolksy et al. 2003). Recent reviews on the jet/wind-disc connection can be found in Königl & Pudritz (2000) and Pudritz & Banerjee (2005). Clearly there are several alternative outflow scenarios. Here we adopt a simple kinematical model, based on the disc-wind paradigm, which broadly represents the results of MHD simulations,

Knigge, Woods, & Drew (1995) introduced the “split-monopole” kinematic disc-wind model in their studies of the UV resonance lines formed in the winds of cataclysmic variable stars. His formalism provides a simple parameterisation of a disc wind that has similar properties to those found by MHD modelling. In this model, the outflow arises from the surface of the rotating accretion disc, and has a biconical geometry. The specific angular momentum is assumed to be conserved along a stream line, and the poloidal velocity component is assumed to be simply a radial from

vertically displaced “sources” from the central star. Here we briefly describe the disc-wind model, and readers are referred to Knigge et al. (1995) and Long & Knigge (2002) for details.

The four basic parameters of the model are: (1) the mass-loss rate, (2) the degree of the wind collimation, (3) the velocity gradient, and (4) the wind temperature. The basic configuration of the disc-wind model is shown in Figure 1. The disc wind originates from the disc surface, but the “source” point ( $S$ ), from which the stream lines diverges, are placed at distance  $d$  above and below the centre of the star. The angle of the mass-loss launching from the disc is controlled by changing the value of  $d$ . The mass-loss launching occurs between  $R_{wi}$  and  $R_{wo}$  where the former is set to be equal to the outer radius of the magnetosphere ( $R_{\text{mo}}$ ) and the latter is set to 1 au as in Krasnopolksy et al. (2003).

The local mass-loss rate per unit area ( $\dot{m}$ ) is assumed to be proportional to the mid-plane temperature of the disc, and is a function of the cylindrical radius  $w = (x^2 + y^2)^{1/2}$ , i.e.

$$\dot{m}(w) \propto T(w)^\alpha . \quad (2)$$

The mid-plane temperature of the disc is assumed to be expressed as a power-law in  $w$ ; thus,  $T \propto w^q$ . Using this in the relation above, one finds

$$\dot{m}(w) \propto w^p \quad (3)$$

where  $p = \alpha \times q$ . The index of the mid-plane temperature power law is adopted from the dust radiative transfer model of Whitney et al. (2003) who found the innermost part of the accretion disc has  $q = -1.15$ . In order to be consistent with the collimated disc-wind model of Krasnopolsky et al. (2003) who used  $p = -3/2$ , the value of  $\alpha$  is set to 1.3. The constant of proportionality in equation 3 is found by integrating  $\dot{m}$  from  $R_{\text{wi}}$  to  $R_{\text{wo}}$ , and the normalising the value to the total mass-loss rate  $\dot{M}_{\text{wind}}$ .

The azimuthal/rotational component of the wind velocity  $v_\phi(w, z)$  is computed from the Keplerian rotational velocity at the emerging point of the stream line i.e.  $v_\phi(w_i, 0) = (GM_*/w_i)^{1/2}$  where  $w_i$  is the distance from the rotational axis ( $z$ ) to the emerging point on the disc, and by assuming the conservation of the specific angular momentum along a stream line:

$$v_\phi(w, z) = v_\phi(w_i, 0) \left( \frac{w_i}{w} \right) . \quad (4)$$

Based on the canonical  $\beta$  velocity law of hot stellar winds (c.f. Castor, Abbott, & Klein 1975), the poloidal component of the wind velocity ( $v_p$ ) parameterised as:

$$v_p(w_i, l) = c_s(w_i) + [f v_{\text{esc}} - c_s(w_i)] \left( 1 - \frac{R_s}{l + R_s} \right)^\beta \quad (5)$$

where  $c_s$ ,  $f$ , and  $l$  are the sound speed at the wind launching point on the disc, the constant scale factor of the asymptotic terminal velocity to the local escape velocity (from the wind emerging point on the disc), and the distance from the disc surface along stream lines respectively.  $R_s$  is the wind scale length, and its value is set to 10  $R_{\text{mi}}$  by following Long & Knigge (2002).

Assuming mass-flux conservation and using the velocity field defined above, the disc wind density as a function of  $w$  and  $l$  can be written as

$$\rho(w_i, l) = \frac{\dot{m}(w_i)}{v_p(w_i, l) |\cos \delta|} \left\{ \frac{d}{D(w_i, l) \cos \delta} \right\}^2 \quad (6)$$

where  $D$  and  $\delta$  are the distance from the source point ( $S$ ) to a point along the stream line and the angle between the stream line and the disc normal, respectively. Figure 2 shows the density and the velocity components along the mid stream line (passing through  $w_i = (R_{\text{wi}} + R_{\text{wo}})/2$  on the disc plane ( $z = 0$ ) for different values of the wind acceleration parameter  $\beta$ .

## 2.4 The accretion disc

We adopt a simple analytical accretion disc model, the  $\alpha$ -disc ‘standard model’ (Shakura & Sunyaev 1973; Frank, King, & Raine 2002) with the inner radius fixed at the inner radius of the magnetosphere at equatorial plane. This corresponds to Region 4 in Fig. 1.

### 2.4.1 Density and velocity

The disc density distribution is given by

$$\rho_d(w, z) = \Sigma(w) \frac{1}{\sqrt{2\pi} h(w)} e^{-\left(\frac{z}{2h(w)}\right)^2} \quad (7)$$

where  $w = \sqrt{x^2 + y^2}$ ,  $h$ ,  $z$  and  $\Sigma$  are the distance from the symmetry axis, the scale height, the distance from the disc plane, and the surface density at the mid-plane, respectively. The mid-plane surface density and the scale height are given as:

$$\Sigma(w) = \frac{5M_d}{8\pi R_{\text{do}}^2} w^{-3/4} \quad (8)$$

where  $R_{\text{do}}$  and  $M_d$  are the disc radius and the disc mass respectively.

$$h(w) = 0.05 R_{\text{do}} w^{9/8} . \quad (9)$$

With these parameters, the disc is slightly flared. The inner radius of the disc is set to  $R_{\text{di}} = R_{\text{mi}}$ . The disc mass,  $M_d$ , is assumed to be 1/100 of the stellar mass ( $M_*$ ), and the outer disc radius ( $R_{\text{di}}$ ) is 100 au. The velocity of the gas/dust in the disc is assumed to be Keplerian.

Because of the geometrical constraints imposed by the magnetosphere and the disc wind, the finite height of the  $\alpha$  disc causes an undesirable interface problem at the boundary; hence, the inner part ( $R_{\text{di}} < w < R_{\text{wo}}$ ) of the disc is replaced by the geometrically thin (but opaque) disc. Since the emissivity of the disc at optical wavelengths is negligible, and the disc scale height is relatively small in the inner part of disc, this simplification is reasonable: the most important factor in determining the shape of the H $\alpha$  profiles is the finite height of the disc at large radii for large inclinations.

### 2.4.2 Dust model

In order to calculate the dust scattering and absorption cross section as a function of wavelength, the optical constants of Draine & Lee (1984) for amorphous carbon grains and Hanner (1988) for silicate grains are used. The model uses the “large grain” dust model of Wood et al. (2002) in which the dust grain size distribution is described by the following function:

$$n(a) da = (C_C + C_{\text{Si}}) a^{-p} \exp \left[ -\left( \frac{a}{a_c} \right)^q \right] da \quad (10)$$

where  $a$  is the grain size restricted between  $a_{\min}$  and  $a_{\max}$ , and  $C_C$  and  $C_{\text{Si}}$  are the terms set by requiring the grains to completely deplete a solar abundance carbon and silicon. The parameters adopted in our model are:  $C_C = 1.32 \times 10^{-17}$ ,  $C_{\text{Si}} = 1.05 \times 10^{-17}$ ,  $p = 3.0$ ,  $q = 0.6$ ,  $a_{\min} = 0.1 \mu\text{m}$ ,  $a_{\max} = 1000 \mu\text{m}$ , and  $a_c = 50 \mu\text{m}$ . This corresponds to Model 1 of the dust model used by Wood et al. (2002). See also their Fig. 3. The relative numbers of each grain is assumed to be that of solar abundance, C/H  $\sim 3.5 \times 10^{-4}$  (Anders & Grevesse 1989) and Si/H  $\sim 3.6 \times 10^{-5}$  (Grevesse & Noels 1993) which are similar to values found in the ISM model of Mathis, Rumpl, & Nordsieck (1977) and Kim, Martin, & Hendry (1994).

## 3 THE RADIATIVE TRANSFER MODEL

We have extended the TORUS radiative transfer code (Harries 2000; Kurosawa et al. 2004; Symington et al. 2005a) to include the multiple circumstellar components described above. In previous calculations (Symington et al. 2005a), the model was used with a three-dimensional (3-D) adaptive mesh refinement (AMR) grid to investigate the line variability associated with rotational modulation of complex geometrical configurations of magnetospheric inflow (see also Kurosawa, Harries, & Symington 2005). We modified the code to handle the a two-dimensional (2-D) density distribution, and restricted our models to be axi-symmetric. Note that the

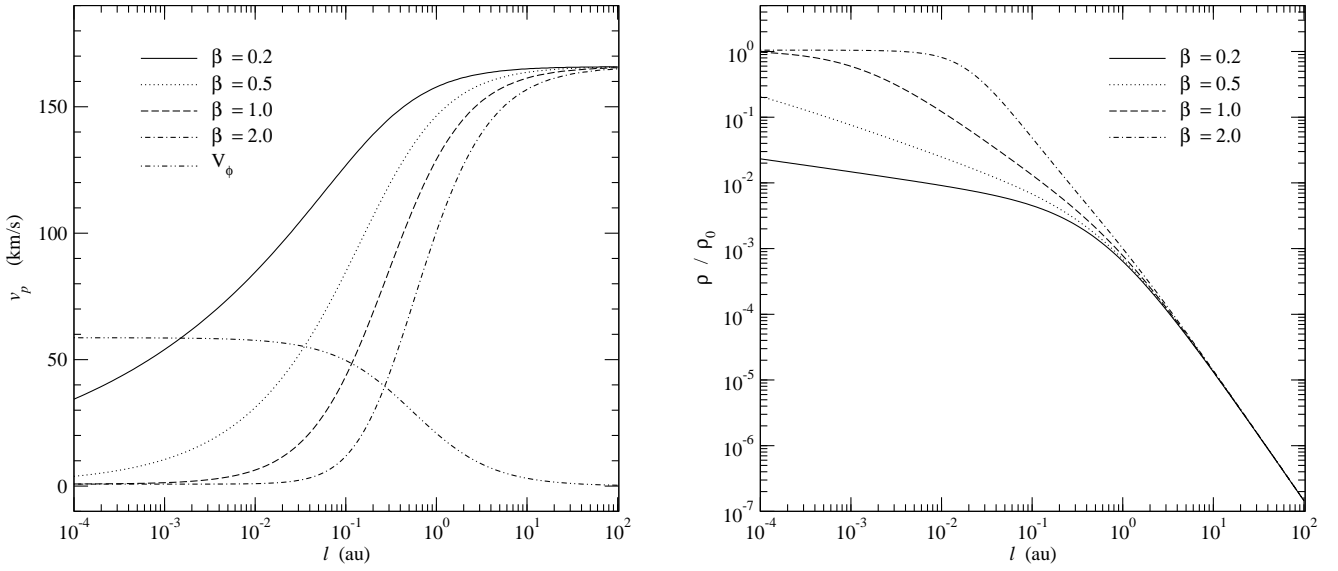


**Figure 2.** The dependency of the disc-wind density and velocity on the wind acceleration parameter  $\beta$ . The wind density  $\rho$  (left panel) and the poloidal velocity component  $v_p$  (right panel) along the stream line starting from the mid point of the wind launching zone, i.e.  $(w, z) = (w_{\text{mid}}, 0)$  where  $w_{\text{mid}} = (R_{\text{wi}} + R_{\text{wo}})/2$ , are shown as a function of the distance ( $l$ ) from the wind launching point (c.f. equations 5 and 6). The azimuthal velocity component ( $v_\phi$ ), which is independent of  $\beta$  (c.f. equation 4), is also shown in the right panel for comparison. The density is normalised to the density  $\rho_0$  at the wind launching point for the  $\beta = 1.0$  case. The  $v_p$  reaches the terminal velocity by 100 au for all  $\beta$ . In the far field ( $l > 10$  au), the density is approximately proportional to  $\sim l^2$ .

velocity field is still in 3-D – the third component can be calculated by using symmetry for a given value of azimuthal angle.

The computation of H $\alpha$  is divided in two parts: (1) the source function calculation ( $S_\nu$ ) and (2) the observed flux/profile calculation. In the first process, we have used the method of Klein & Castor (1978) (see also Rybicki & Hummer 1978; Hartmann et al. 1994) in which the Sobolev approximation method is applied. The population of the bound states of hydrogen are assumed to be in statistical equilibrium, and the gas to be in radiative equilibrium. Our hydrogen atom model consist of 14 bound states and a continuum. Readers are refer to Harries (2000) for details.

Monte Carlo radiative transfer (e.g. Hillier 1991), under the Sobolev approximation, can be used when (1) a large velocity gradient is present in the gas flow, and (2) the intrinsic line width is negligible compared to the Doppler broadening of the line. In our earlier models (Harries 2000; Symington et al. 2005a), this method was adopted since these conditions are satisfied. However, as noted and demonstrated by Muzerolle et al. (2001), even with a moderate mass-accretion rate ( $10^{-7} \text{ M}_\odot \text{ yr}^{-1}$ ), Stark broadening becomes important in the optically thick H $\alpha$  line. Muzerolle et al. (2001) also pointed out that the observed H $\alpha$  profiles from CTTS typically have the wings extending to 500 km s $^{-1}$  (e.g. Edwards et al. 1994; Reipurth et al. 1996) which cannot be explained by the infall velocity alone.

We have implemented the broadening mechanism following the formalism described by Muzerolle et al. (2001). First, the emission and absorption profiles are replaced from the Doppler to the Voigt profile, which is defined as:

$$H(a, y) \equiv \frac{a}{\pi} \int_{-\infty}^{\infty} \frac{e^{-y'^2}}{(y - y')^2 + a^2} dy' \quad (11)$$

where  $a = \Gamma/4\pi\Delta\nu_D$ ,  $y = (\nu - \nu_0)/\Delta\nu_D$ , and  $y' = (\nu' - \nu_0)/\Delta\nu_D$  (c.f. Mihalas 1978).  $\nu_0$  is the line centre frequency, and  $\Delta\nu_D$  is the Doppler line width of hydrogen atom (due

to its thermal motion) which is given by  $\Delta\nu_D = (2kT/m_H)^{1/2} \times (\nu_0/c)$  where  $m_H$  is the mass of a hydrogen atom. The damping constant  $\Gamma$ , which depends on the physical condition of the gas, is parameterised by Vernazza, Avrett, & Loeser (1973) as follows:

$$\begin{aligned} \Gamma = & C_{\text{rad}} + C_{\text{vdW}} \left( \frac{n_{\text{HI}}}{10^{16} \text{ cm}^{-3}} \right) \left( \frac{T}{5000 \text{ K}} \right)^{0.3} \\ & + C_{\text{Stark}} \left( \frac{n_e}{10^{12} \text{ cm}^{-3}} \right)^{2/3} \end{aligned} \quad (12)$$

where  $n_{\text{HI}}$  and  $n_e$  are the number density of neutral hydrogens and that of free electrons. Also,  $C_{\text{rad}}$ ,  $C_{\text{vdW}}$  and  $C_{\text{Stark}}$  are natural broadening, van der Waals broadening, and linear Stark broadening constants respectively. We simply adopt this parameterisation along with the values of broadening constants for H $\alpha$  from Luttermoser & Johnson (1992), i.e.  $C_{\text{rad}} = 6.5 \times 10^{-4} \text{ \AA}$ ,  $C_{\text{vdW}} = 4.4 \times 10^{-4} \text{ \AA}$  and  $C_{\text{Stark}} = 1.17 \times 10^{-3} \text{ \AA}$ . In terms of level populations and the Voigt profile, the line opacity for the transition  $i \rightarrow j$  can be written as:

$$\chi_i = \frac{\pi^{1/2} e^2}{m_e c} f_{ij} n_j \left( 1 - \frac{g_j n_i}{g_i n_j} \right) H(a, y) \quad (13)$$

where  $f_{ij}$ ,  $n_i$ ,  $n_j$ ,  $g_i$  and  $g_j$  are the oscillator strength, the population of  $i$ -th level, the population of  $j$ -th level, the degeneracy of the  $i$ -th level, and the degeneracy of the  $j$ -th level respectively.  $m_e$  and  $e$  are the electron mass and charge (c.f. Mihalas 1978).

We further modified TORUS by replacing the Monte Carlo line transfer algorithm with a direct integration method (c.f. Mihalas 1978) for computing the observed flux as a function of frequency. The integration of the flux is performed in the cylindrical coordinate system  $(p, q, t)$  which is obtained by rotating the original stellar coordinate system  $(\rho, \phi, z)$  around the  $y$  axis by the inclination of the line of sight. Note that the  $t$ -axis coincides with the line of sight with this rotation. The observed flux ( $F_\nu$ ) is given by:

$$F_\nu = \frac{1}{4\pi d^2} \int_0^{p_{\max}} \int_0^{2\pi} p \sin q I_\nu dq dp \quad (14)$$

where  $d$ ,  $p_{\max}$ , and  $I_\nu$  are the distance to an observer, the maximum extent to the model space in the projected (rotated) plane, and the specific intensity ( $I_\nu$ ) in the direction on observer at the outer boundary. For a given ray along  $t$ , the specific intensity is given by:

$$I_\nu = I_0 e^{-\tau_\infty} + \int_{t_0}^{t_\infty} S_\nu(t) e^{-\tau} dt \quad (15)$$

where  $I_0$  and  $S_\nu$  are the intensity at the boundary on the opposite to the observer and the source function ( $\eta_\nu/\chi_\nu$ ) of the stellar atmosphere/wind at a frequency  $\nu$ . For a ray which intersects with the stellar core,  $I_0$  is computed from the stellar atmosphere model of Kurucz (1979) as described in section 2.1, and  $I_0 = 0$  otherwise. If the ray intersects with the hot ring on the stellar surface created by the accretion stream, we set  $I_0 = B_\nu(T_{\text{ring}})$  where  $B_\nu$  is the Planck function and  $T_{\text{ring}}$  is the temperature of the hot ring. The initial position of each ray is assigned to be at the centre of the surface element ( $dA = p \sin q dq dp$ ). The code execution time is proportional to  $n_p n_q n_\nu$  where  $n_p$  and  $n_q$  are the number of cylindrical radial and angular points for the flux integration, and  $n_\nu$  is the number of frequency points. In the models presented in the following section,  $n_p = 180$ ,  $n_q = 100$ , and  $n_\nu = 101$  are used unless specified otherwise. A linearly spaced radial grid is used for the area where the ray intersects with magnetosphere, and a logarithmically spaced grid is used for the wind and the accretion disc regions.

The optical depth  $\tau$  is equation 15 is defined as:

$$\tau(t) \equiv \int_t^\infty \chi_\nu(t') dt'$$

where  $\chi_\nu$  is the opacity of media the ray passes through.  $\tau_\infty$  is the total optical depth measured from the initial ray point to the observer (or to the outer boundary closer to the observer). Initially, the optical depth segments  $d\tau$  are computed at the intersections of a ray with the original AMR grid in which the opacity and emissivity information are stored. For high optical depth models, additional points are inserted between the original points along the ray, and  $\eta_\nu$  are  $\chi_\nu$  values are interpolated to those points to ensure  $d\tau < 0.05$  for all ray segments.

For a point in the magnetosphere and the wind flows, the emissivity and the opacity of the media are given as:

$$\begin{cases} \eta_\nu &= \eta_c^H + \eta_l^H \\ \chi_\nu &= \chi_c^H + \chi_l^H + \sigma_{\text{es}} \end{cases} \quad (16)$$

where  $\eta_c^H$  and  $\eta_l^H$  are the continuum and line emissivity of hydrogen.  $\chi_c^H$ ,  $\chi_l^H$ , and  $\sigma_{\text{es}}$  are the continuum, line opacity (equation 13) of hydrogen, and the electron scattering opacity. Similarly, for a point in the accretion disc,

$$\begin{cases} \eta_\nu &= 0 \\ \chi_\nu &= \kappa_{\text{abs}}^{\text{dust}} + \kappa_{\text{sca}}^{\text{dust}} \end{cases} \quad (17)$$

where  $\kappa_{\text{abs}}^{\text{dust}}$  and  $\kappa_{\text{sca}}^{\text{dust}}$  are the dust absorption, and scattering opacity which are calculated using the dust property described in section 10. We neglect the emissivity from the disc: since the disc mass of CTTS are rather small ( $\sim 0.01 M_\odot$ ) and low temperature ( $\lesssim 1600$  K), the continuum flux contribution at H $\alpha$  wavelength is expected to be negligible (e.g. Chiang & Goldreich 1997).

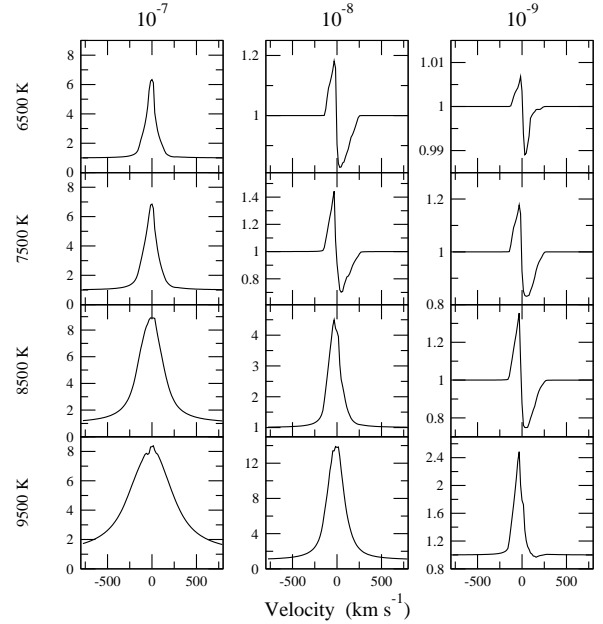


**Figure 3.** H $\alpha$  model profiles for wide ranges of mass accretion rate ( $\dot{M}_{\text{acc}}$ ) and temperature ( $T_{\max}$ ). The profiles are computed using only the magnetospheric accretion flow (i.e. no outflow). All the profiles are computed using the parameters of the reference model (Table 1) and inclination  $i = 55^\circ$ . The temperature (indicated along the vertical axis) of the model increases from top to bottom, and the mass accretion rate (indicated by the values in  $M_\odot \text{ yr}^{-1}$  along the top) increases from left to right.

## 4 RESULTS

### 4.1 Magnetosphere only models

Using the reference model parameters (Table 1) for the central star and the magnetosphere, we examine the dependency of H $\alpha$  on the temperature ( $T_{\max}$ ) of accretion flow and the mass accretion rate ( $\dot{M}_{\text{acc}}$ ), as done by Muzerolle et al. (2001) for H $\beta$ . We note that here we have computed the hot ring temperature self-consistently, whereas Muzerolle et al. (2001) used a constant hot ring temperature (8000 K) for most of their models. The accretion luminosity ( $L_{\text{acc}}$ ) for models with  $\dot{M}_{\text{acc}} = 10^{-7} M_\odot \text{ yr}^{-1}$  is about a half of the photospheric luminosity.

H $\alpha$  line profiles for a range of  $T_{\max}$  and  $\dot{M}_{\text{acc}}$  are presented in Figure 3. The overall dependency on  $T_{\max}$  and  $\dot{M}_{\text{acc}}$  is similar to that of Muzerolle et al. (2001). In general, the line strength weakens as the accretion rate and the temperature drop. The red-shifted absorption becomes less visible for the higher accretion rate and higher temperature models as it becomes filled-in by the stronger Stark-broadened line-wing emission.

We demonstrate this effect in Figure 4, which shows an example for an H $\alpha$  model with  $T_{\max} = 7500$  K and  $\dot{M}_{\text{acc}} = 10^{-7} M_\odot \text{ yr}^{-1}$ , both with and without damping. Although the maximum flux of the model with broadening is almost identical to that of the model with no damping constant ( $\Gamma = 0$ ), a significant increase of the line flux in both red and blue wings is seen. The weak red-shifted absorption component (which is a signature of the magnetospheric accretion) is weakened or eliminated by the flux in broadened wing.

Table 2 shows the equivalent width (EW) for the models in Figure 3. The EWs for half the models fall within the range of EWs ( $\sim 3 \text{ \AA}$  to  $\sim 160 \text{ \AA}$ ) measured by Alencar & Basri (2000). The

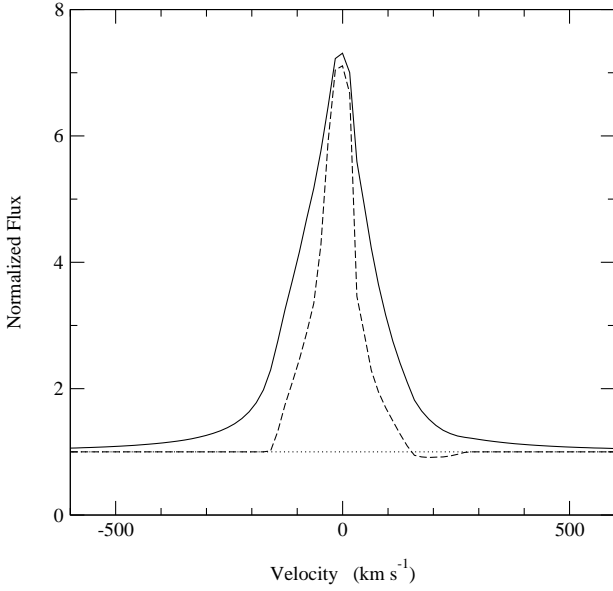


**Figure 4.** The effect of line broadening on H $\alpha$ . A model computed with a damping constant ( $\Gamma$ ), described in section 3 (solid), is compared with a model with no damping,  $\Gamma = 0$  (dashed). Both models are computed with  $T_{\text{max}} = 7500$  K,  $i = 55^\circ$ , and the reference parameters given in Table 1. The two models have similar peak flux levels (around  $V \sim 0$  km s $^{-1}$ ), but the total flux and the EW of the line increased drastically for the model with the damping constant. The broad wings extend to  $\sim \pm 800$  km s $^{-1}$ . The redshifted absorption feature (very weakly) seen in the  $\Gamma = 0$  model is not seen in the model with the broadening.

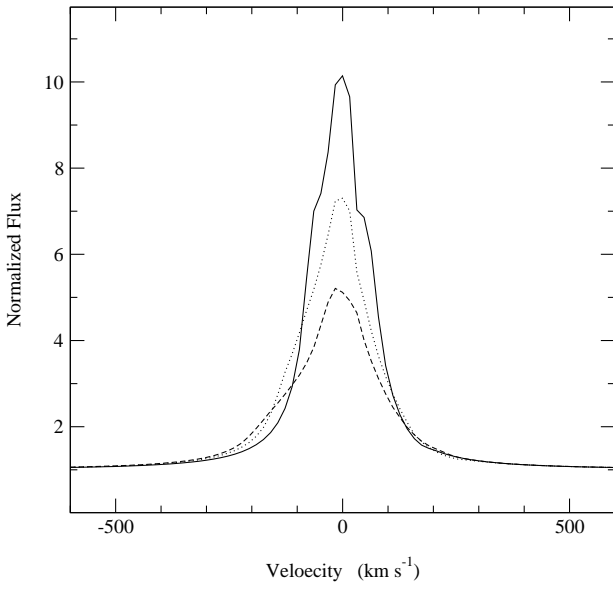


**Figure 5.** The dependency of the H $\alpha$  profile on inclination ( $i$ ). The profiles are computed with a magnetospheric accretion flow only using the reference parameters given in Table 1 and  $T_{\text{max}} = 7500$  K. The solid, dotted, and dashed lines are for  $i = 10^\circ$ ,  $55^\circ$ , and  $80^\circ$  respectively. As the inclination becomes larger, the peak flux and the equivalent width of the line becomes smaller.

**Table 2.** Summary of H $\alpha$  equivalent widths ( $\text{\AA}$ ) from the magnetospheric accretion flow models shown in Figure 3. Note that the equivalent widths are positive when the lines are in emission.

$T_{\text{max}}$ (K)	$\dot{M}_{\text{acc}}$ ( $M_\odot \text{yr}^{-1}$ )		
	$10^{-7}$	$10^{-8}$	$10^{-9}$
6500	17.9	0.1	0.0
7500	25.2	-0.9	-0.5
8500	68.3	6.5	-0.7
9500	98.6	52.4	1.3

EWs of models with the lowest mass accretion rates fall below the minimum EW observed by Alencar & Basri (2000), while several models would be designated as weak-lined T Tauri stars (WTTS) using the traditional 10 Å cut-off (e.g. Herbig & Bell 1988). White & Basri (2003) empirically showed that the full width of H $\alpha$  at 10 per cent of its peak flux (10 per cent width) is a better indicator for an accretion than the EW criteria. They proposed that a T Tauri star shows the 10 per cent width greater than 270 km s $^{-1}$ , the star should be a CTTS. The 10 per cent widths of the model H $\alpha$  profiles (Figure 3) are summarised in Table 3. Using the criteria of White & Basri (2003), the half of the models shown in the figure can be classified as CTTS, and the other half as WTTS. However, the profiles corresponding to the WTTS designations have an inverse P-Cygni morphology that is rarely seen in observations (Reipurth et al. 1996 and section 5.1).

The dependency of the line profile on inclination angle ( $i$ ) is demonstrated in Figure 5. The model has  $T_{\text{max}} = 7500$  K and  $\dot{M}_{\text{acc}} = 10^{-7} M_\odot \text{yr}^{-1}$ ). The figure shows that the peak (normalised) flux decreases as the inclination angle increases, as does the EW. The line flux and the EWs decrease mainly because the fraction of the accretion stream blocked by the photosphere increases as the inclination increases. The line EW in Figure 5 changes from 32 Å to 21 Å as the inclination changes from  $10^\circ$  to  $80^\circ$ , i.e. the fractional change of 0.65. On the other hand, the 10 per cent width of the line changes from 290 km s $^{-1}$  to 470 km s $^{-1}$ ; hence, the fractional change is 1.6. The both values are relatively sensitive to the inclination angle.

Because of the geometry of the magnetospheric accretion (c.f. Figure 1) and of the presence of the gas with the highest velocity close to the stellar surface, the highest red-shifted line-of-sight velocity is visible only at the high inclination angles. This explains the wider appearance of the profile with  $i = 80^\circ$  compared to the relatively narrow line appearance of the profile with  $i = 10^\circ$ . A similar EW dependence on inclination angle is found for the models with different magnetospheric temperatures and the mass-accretion rates.

Our models show a blue-shifted line peak and a blueward asymmetry caused by occultation of the accretion flow by the stellar photosphere (see also Hartmann et al. 1994; Muzerolle et al. 2001). However, Alencar & Basri 2000 (see their Fig. 9) found a substantial fraction of the observed H $\alpha$  profiles show a red-shifted peak. Furthermore, a recent study by Appenzeller et al. (2005) demonstrated that the equivalent width of H $\alpha$  from CTTS *increases* as the inclination angle increases. Clearly a magnetospheric accretion only model cannot explain the full properties of the H $\alpha$  profiles in CTTS.

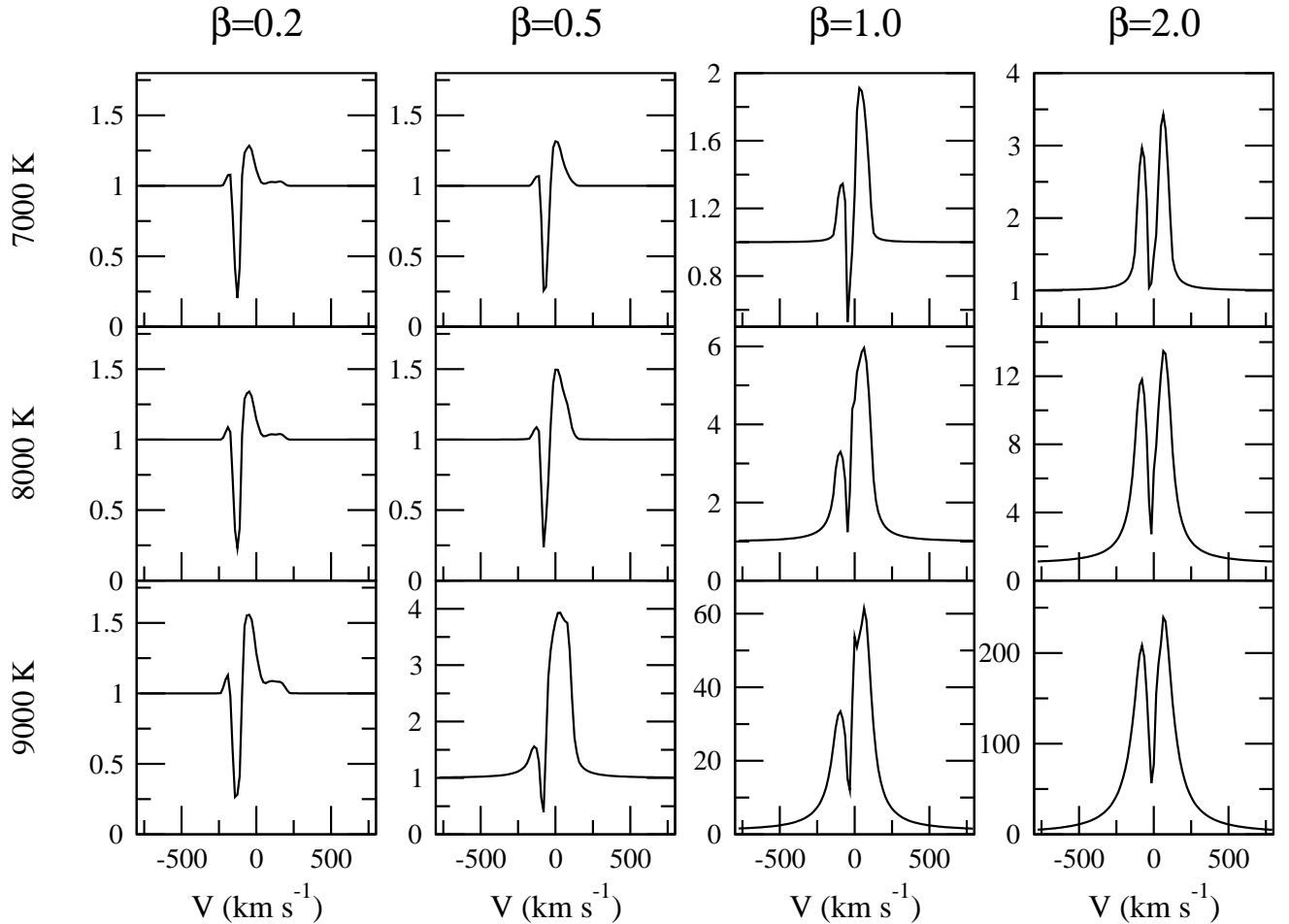


**Figure 6.** H $\alpha$  profiles computed with the disc-wind only. The wind mass-loss rate is fixed at  $\dot{M}_{\text{wind}} = 10^{-8} M_{\odot} \text{ yr}^{-1}$ , and the line profiles are computed with different combinations of the wind acceleration rate ( $\beta$ ) and isothermal disc-wind temperature ( $T_{\text{wind}}$ ). The wind emission grows as the values of  $\beta$  and  $T_{\text{wind}}$  increase. The position of the wind absorption moves toward the line centre as  $\beta$  becomes larger.

**Table 3.** Summary of 10 per cent widths ( $\text{km s}^{-1}$ ) from the magnetospheric accretion flow models shown in Figure 3.

$T_{\text{max}}$ (K)	$\dot{M}_{\text{acc}}$ ( $M_{\odot} \text{ yr}^{-1}$ )		
	$10^{-7}$	$10^{-8}$	$10^{-9}$
6500	300	120	100
7500	360	145	120
8500	790	330	130
9500	1530	520	200

#### 4.2 Disc-wind only models

In this section, we examine profiles produced using the the disc wind outflow model described in section 2.3. The parameters used for the central star are as in section 2.1, and the disc-wind parameters are summarised in Table 4. Although the line is potentially sensitive to the temperature structure of the wind, determination of a self-consistent wind temperature is beyond the scope of this paper. Readers are referred to Hartmann et al. (1982) in which the wind temperature structure is determined by balancing the radiative

cooling rate (assuming optically thin) with the MHD wave heating rate. We pragmatically assume that the wind is isothermal at  $T_{\text{wind}}$ .

Initially we examine the characteristics of the H $\alpha$  profile as a function of the wind acceleration parameter  $\beta$  and the isothermal wind temperature  $T_{\text{wind}}$ . The mass-loss rate is kept constant at  $\dot{M}_{\text{wind}} = 10^{-8} M_{\odot} \text{ yr}^{-1}$ . Figure 6 shows the model profiles computed for the wind temperatures between 7000 K and 9000 K, and those with  $\beta$  between 0.2 and 2.0, computed at inclination  $i = 55^\circ$ . The morphology of the profile exhibited by the model changes from FU-Ori type (c.f. Reipurth et al. 1996) for the models with small  $\beta$  to the stronger emission types, which are more commonly seen in the observed H $\alpha$  (c.f. Reipurth et al. 1996), as the value of  $\beta$  increases. Classical P Cygni profiles are prominent in the models with lower values of  $T_{\text{wind}}$  and  $\beta$  (a colder and faster accelerating wind). As the value of  $\beta$  increases, the position of the blue-shifted absorption component moves toward the line centre. The blue edge of the absorption component in the fastest accelerating wind ( $\beta = 0.2$ ) model is almost at the terminal velocity ( $v_{\infty} \sim 160 \text{ km s}^{-1}$ ) of the disc wind (c.f. Figure 2), that for the slowest wind acceleration model ( $\beta = 4.0$ ) is located close the line centre ( $\sim 20 \text{ km s}^{-1}$ ).

The intensity of the emission component increases as  $\beta$  increases for a fixed  $T_{\text{wind}}$ . This is mainly because the density near the photosphere increases as the value of  $\beta$  increases (Figure 2);

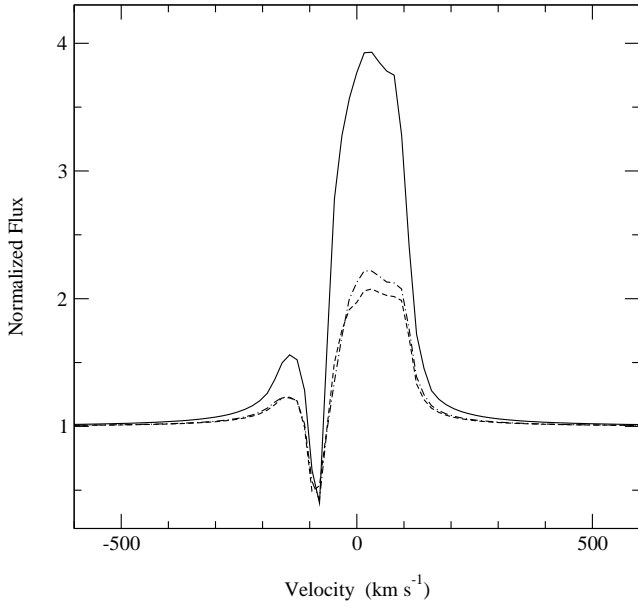


**Figure 7.** The dependency of the H $\alpha$  profile on the source displacement parameter  $d$ . The line profiles are computed with the wind parameter  $T_{\text{wind}} = 9000\text{K}$  and  $\beta = 0.5$  for  $i = 55^\circ$ . The profiles in the figure use  $d = 11 R_*$  (dashed),  $18 R_*$  (dash-dot) and  $22 R_*$  (solid). All the other parameters are same as in Figure 6. As the wind becomes more collimated (larger  $d$ ), the wind launching angle becomes smaller and the wind density is enhanced towards the symmetry axis ( $z$ ); hence, the wind emission increases. The absorption component is relatively insensitive to  $d$  since the change in the column density toward the observer is relatively small.

**Table 4.** A summary of the reference disc-wind model parameters used in section 4.2. See also section 2.3.

$d$ [ $R_*$ ]	$R_{\text{wi}}$ [ $R_*$ ]	$R_{\text{wo}}$ [au]	$\dot{M}_{\text{wind}}$ [ $M_\odot \text{ yr}^{-1}$ ]	$p$ [-]	$f$ [-]	$R_s$ [ $R_*$ ]
22	3.0	1.0	$10^{-8}$	-3/2	2.0	30

hence, the emissivity of increases. Most of the profiles show a redward asymmetry, mainly due to the presence of the classical P-Cygni absorption. However we find that the disc-wind models with the fastest acceleration ( $\beta = 0.2$  and  $0.5$ ) and viewed at low inclinations, show a strong blue asymmetry due to occultation of the receding half of the outflow by the optically thick disc.

The effect of varying the wind mass-loss rate is shown in Figure 8. With all other parameters fixed,  $\dot{M}_{\text{wind}}$  acts as an scaling factor for the wind density (equation 6). The important process that populates the  $n = 3$  level is recombination, and therefore the line emissivity varies as the square of the density (assuming that the ionisation fraction remains constant); hence the line is very sensitive to changes in  $\dot{M}_{\text{wind}}$ . We indeed find that the line flux of the models is approximately proportional to the square of the mass-loss rate.

#### 4.3 Disc-wind-magnetosphere hybrid models

We now consider models computed with a combination of the disc-wind and magnetospheric accretion components. The parameters used for the magnetosphere are same as in Figure 5, and

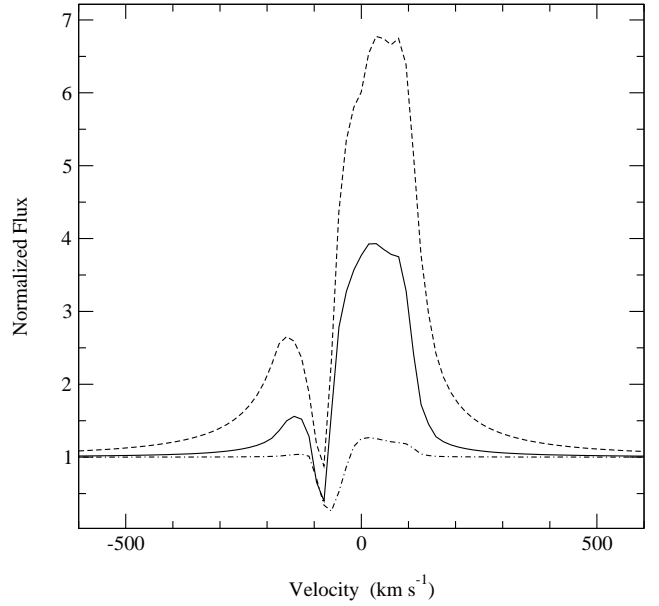


**Figure 8.** The effect of the wind mass-loss rate. The profiles computed with  $(T_{\text{wind}}, \beta) = (9000\text{K}, 0.5)$ , and  $\dot{M}_{\text{wind}} = 2.0 \times 10^{-8} M_\odot \text{ yr}^{-1}$  (dashed),  $1.0 \times 10^{-8} M_\odot \text{ yr}^{-1}$  (solid), and  $0.5 \times 10^{-8} M_\odot \text{ yr}^{-1}$  (dash-dot) are shown above. With all other parameter fixed, the mass-loss rate behaves as a scaling factor for the wind density (c.f. equation 6).

the mass-loss rate of the disc wind is  $\dot{M}_{\text{wind}} = 10^{-8} M_\odot \text{ yr}^{-1}$  (i.e.  $\mu = \dot{M}_{\text{wind}}/\dot{M}_{\text{acc}} = 0.1$ ). Figure 9 shows the models profiles computed using the same ranges of the disc-wind temperature and wind acceleration parameter as in the previous cases.

As in the disc-wind only models (Figure 6), the location of the absorption component moves toward the line centre as the value of  $\beta$  increases. The figure shows that in the models with smaller  $\beta$  and  $T_{\text{wind}}$ , the line emission from the magnetosphere dominates, while this situation reverses for the models with larger  $\beta$  and  $T_{\text{wind}}$ . The model with  $(T_{\text{wind}}, \beta) = (9000\text{K}, 2.0)$  results in an H $\alpha$  profile that is far too strong to be compatible with observations (Reipurth et al. 1996 and Alencar & Basri 2000); however, the lower mass-loss rate models (while keeping  $\mu$  constant) produce profiles with the line strengths comparable to observations. Although the models in Figure 9 are computed with limited ranges of  $T_{\text{wind}}$ ,  $\beta$  and a fixed  $i$ , the resulting profiles exhibit a wide variety of line profile shapes, many of which are similar to the types of H $\alpha$  profiles seen in the observations (c.f. Reipurth et al. 1996).

In order to quantify the relative contributions of the wind emission and the magnetosphere, we have computed the ratio the EW of the hybrid model in Figure 9 to the EW of the magnetosphere only model (Table 5). This ratio falls below 1.0 when the wind only contributes to the line absorption, but not to the emission. In some models (e.g. with  $T_{\text{wind}} = 8000\text{K}$  and  $\beta = 2.0$ ), the contribution of the wind to the EW is much larger than that of the magnetosphere (EW ratio is 3.2). This clearly demonstrates that the difficulty of using the EW of H $\alpha$  alone as an accretion measure. We have also seen in Figure 6 that disc wind models without a magnetosphere can produce an H $\alpha$  line with significantly large EW.

An examination of the profiles in Figures 6 and Figure 9 reveals some of problems with uniqueness that must inevitably occur when trying to assign an individual profile as wind or accretion dominated i.e. very similar profiles may arise from very different circumstellar geometries. For example, the disc-wind only model

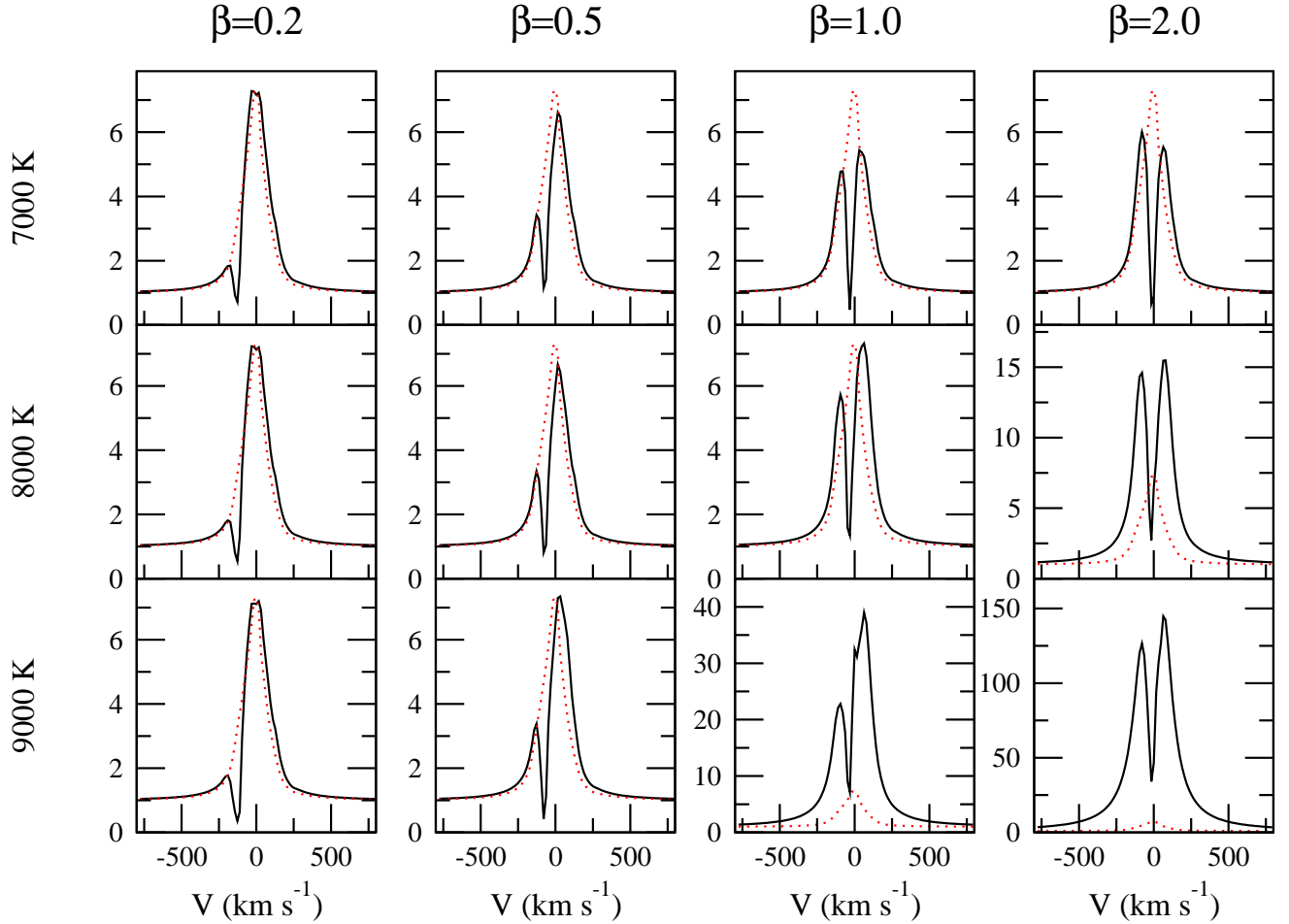


**Figure 9.** The disc-wind-magnetosphere hybrid model. These models (solid lines) have the same parameters as Figure 6, but also include the magnetospheric accretion flow ( $T_{\max} = 7500$  K and  $\dot{M}_{\text{acc}} = 10^{-7} M_{\odot} \text{ yr}^{-1}$ ). While the emission from the magnetosphere dominates for the models with smaller  $\beta$  and  $T_{\text{wind}}$ , the emission from the wind dominates the profiles for models with larger  $\beta$  and  $T_{\text{wind}}$ . The contribution of the magnetosphere can be judged from the profiles computed with the magnetosphere only (dotted lines).

with  $(T_{\text{wind}}, \beta) = (8000 \text{ K}, 1.0)$  in Figures 6 and the accretion dominated model with  $(T_{\text{wind}}, \beta) = (9000 \text{ K}, 0.5)$  in Figure 9 give very similar profiles.

The effect of changing the ratio of the wind mass-loss rate to mass-accretion rate ( $\mu = \dot{M}_{\text{wind}}/\dot{M}_{\text{acc}}$ ) is demonstrated in Figure 10. With a fixed value of mass-accretion rate ( $\dot{M}_{\text{acc}} = 10^{-7} M_{\odot} \text{ yr}^{-1}$ ), the mass-loss rate is varied. The figure shows that as  $\mu$  increases the P-Cygni absorption deepens only slightly, and the position of minimum flux in the absorption trough appears to move blue-ward. On the other hand, the flux peak increase and the line wings become stronger as  $\mu$  increases. Although MHD models suggests (e.g. Königl & Pudritz 2000) that  $\mu \sim 0.1$ , the figure suggest that models a relatively wide range of  $\mu$  (e.g. between 0.025 and 0.2 in this case) reproduce the profiles similar to observations.

Apparently, the type of profiles (affected by the blue-shifted absorption feature) seen in this section cannot be explained by the magnetospheric accretion flow alone (e.g. Muzerolle et al. 2001). Comparison of the model profiles with different types of the observed H $\alpha$  profiles will be given in section 5.1.

xxx add a sample halpha image from poster xxxx

xxxx alter text for consistency with above image xxxx

By inspecting the model H $\alpha$  images computed (no shown

here), we have found that the extent of the H $\alpha$  emission region is relatively small i.e.  $h \lesssim 0.2 \text{ au}$  or  $20 R_{\star}$  where  $h$  is the vertical distance from the disc when compared to the spectro-astrometric observations of Takami et al. (2003) for RU Lup and CS Cha which show 1–5 au scale outflows<sup>1</sup>. The extent of the line emission region becomes slightly larger ( $\sim 0.4 \text{ au}$ ) if a slower wind acceleration rate (e.g.  $\beta = 4$ ) is used.

## 5 DISCUSSION

### 5.1 The morphological classification scheme proposed by Reipurth et. al (1996)

Reipurth et al. (1996) proposed a two-dimensional classification of H $\alpha$  emission profiles of T Tauri stars and Herbig Ae/Be stars. Their

<sup>1</sup> Their observations also show some objects (e.g Z CMa and AS 353A) displaying the outflows in larger scale ( $> 50 \text{ au}$ ); however, this could be formed in shocks rather than MHD-wave heating (e.g. Hartmann et al. 1982) or X-ray heating (e.g. Shang et al. 2002).

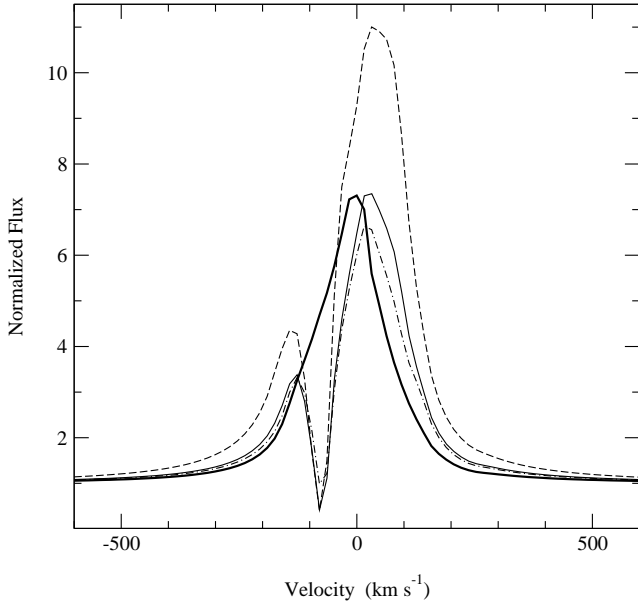


**Figure 10.** The effect of the mass-loss rate to mass-accretion rate ratio ( $\mu = \dot{M}_{\text{wind}}/\dot{M}_{\text{acc}}$ ). The H $\alpha$  profile computed with only the magneto-spheric accretion (thick solid) is compared to the disc-wind-magnetosphere hybrid models for  $\mu = 0.05$  (dash-dot), 0.1 (solid) and 0.2 (dash). The magnetosphere used here has  $T_{\text{max}} = 7500$  K and  $\dot{M}_{\text{acc}} = 10^{-7} M_{\odot}$  yr $^{-1}$ . The temperature and the acceleration parameter of the disc wind are  $T_{\text{wind}} = 9000$  K and  $\beta = 0.5$  respectively. All the models are computed with the inclination angle  $i = 55^\circ$ . As  $\mu$  increases the emission component becomes stronger and the wings becomes broader, as expected. The absorption component is relatively insensitive to the value of  $\mu$  in this example. The wide range of  $\mu$  reasonably reproduces the profiles similar to ones seen in observations (e.g. Reipurth et al. 1996).

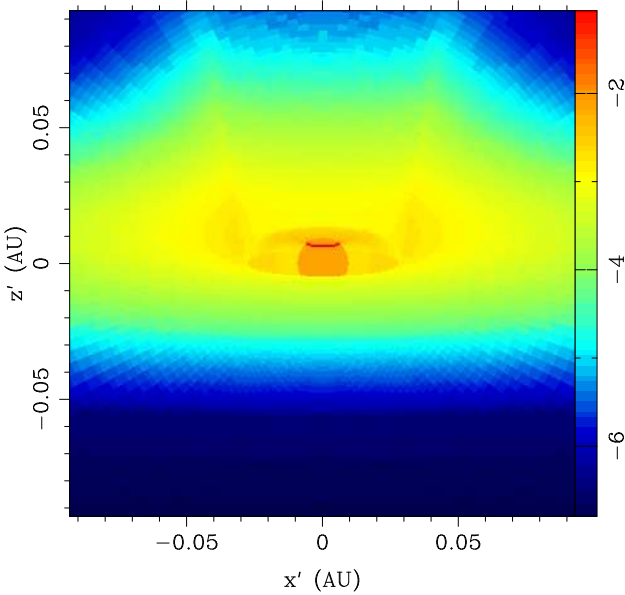


**Figure 11.** An H $\alpha$  image of the disc-wind hybrid model viewed at an inclination of  $80^\circ$ . The false-colour scale shows logarithmic surface brightness (arbitrary units) and the axes are linear dimensions in au.

**Table 5.** The ratio of the line equivalent width (EW) of the disc-wind magnetosphere hybrid models in Figure 9 to the EW of the magnetosphere only model.

$T_{\text{max}}$ (K)	$\beta$				
		0.2	0.5	1.0	2.0
7000		1.1	.94	.89	.96
8000		1.1	.92	1.2	3.2
9000		1.0	1.1	7.5	36.

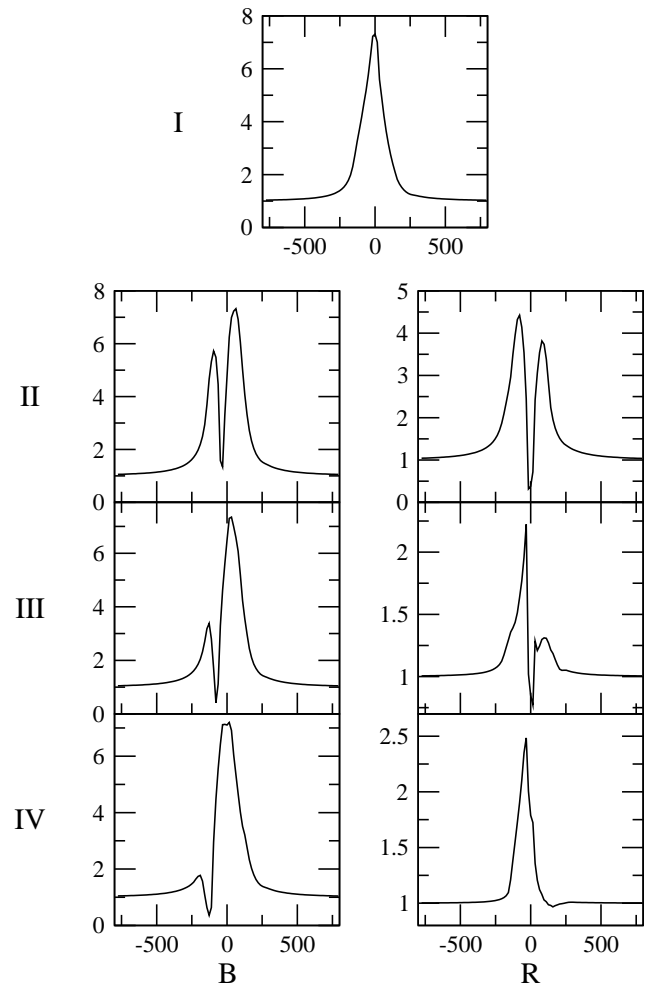


**Figure 12.** Sample H $\alpha$  model profiles which characterise the classification scheme of Reipurth et al. (1996). The combination of magnetospheric accretion flow, the accretion disc, and the disc-wind can reproduce the wide range of H $\alpha$  profiles seen in observations. The model parameters used for each profile along with short comments are given in Table 6. The horizontal axes are velocities in km s $^{-1}$ , and the vertical axes are normalised flux.

classification scheme contains four classes (I, II, III and IV) differentiated by the ratio of the secondary-to-primary emission components in the profiles. Each class is divided into two sub-classes (B and R) which depends whether the secondary peak is on the blue or red side of the primary peak. Readers are referred to Fig. 4 of their paper. Figure 12 shows sample model profiles which are classified according to the definition of Reipurth et al. (1996). The combination of the disc wind, magnetospheric accretion flow, and

the accretion disc can reproduce all the classes of the profiles seen in observations. The corresponding parameters of the disc-wind-magnetosphere hybrid model used to reproduce the profiles in the figure are summarised in Table 6 along with brief comments on possible physical conditions which lead to the profiles in each class. Below we discuss the Reipurth scheme in the context of our models parameters.

#### Type I:

Reipurth et al. (1996) found that Type I profiles (symmetric around line centres) constituted 26 per cent of the 43 CTTS H $\alpha$  profiles in their sample, making it the second most common morphological type. We find that Type I profiles are dominated by magnetospheric emission at rates in excess of  $\approx 10^{-8} M_{\odot} \text{ yr}^{-1}$ . Type I profiles appear at a wide range of inclinations (Figure 5). An object that displays a Type I profile may have relatively weak disc wind, but in this case it must be viewed from the pole (in order that no wind material is seen projected against the stellar photosphere).

#### Type II-B:

These profiles have a secondary blue peak that is in excess of half the strength of the primary peak, and comprised 16 per cent of the Reipurth sample.

This type can be produced by the disc-wind-magnetosphere hybrid models at moderate to high inclination angles with wide ranges of the wind acceleration rate ( $0.2 \lesssim \beta \lesssim 2.0$ ) and the wind temperature ( $7000 \text{ K} \lesssim T \lesssim 9000 \text{ K}$ ). If the inclination is high ( $i \sim 80^\circ$ ), the disc-wind acceleration parameter should be relatively small ( $\beta \lesssim 0.5$ ). If the inclination is moderate ( $i \sim 60^\circ$ ), the wind acceleration parameter should be relatively high ( $\beta \gtrsim 2.0$ ).

#### Type II-R:

These

The physical conditions which result in this type is very similar to those of Type II-B according to the disc-wind-magnetosphere hybrid models. The main difference is between the two is in their inclination angles. This type is more likely seen at higher inclination angles ( $i \sim 80^\circ$ ) compared to Type II-B. Commonly seen in the models with the disc wind only model.

#### Type III-B:

xxx describe this type xxxx

This type is the most commonly seen profiles in the CTTS H $\alpha$  samples in Reipurth et al. (1996). Interestingly, the most common profile type seen in the disc-wind-magnetosphere hybrid model are Type III-B profiles (c.f. Figures 9 and 9). In this type of profiles, the main emission comes from the magnetosphere, and the profile shape is altered from a slightly blue-asymmetric one to a slightly red-asymmetric one via the wind absorption in the blue wing. In the models with the disc-wind, the acceleration parameter should be relatively small ( $\beta < 0.5$ ). The profile type changes from Type III-R to Type II-R if the value of  $\beta$  increases. The inclination angles must be moderate to high ( $60^\circ \lesssim i \lesssim 80^\circ$ ).

#### Type III-R:

xxx describe this type xxxx

This is the least common type of the observed profile (2 per cent) according to Reipurth et al. (1996). Incidentally, we also found it difficult to reproduce this type of profile since this can be achieved only at narrow range of parameter space (very high inclination angle with a disc wind model,  $T_{\max} \sim 8300 \text{ K}$ , and  $\dot{M}_{\text{acc}} \sim 10^{-8} M_{\odot} \text{ yr}^{-1}$ ). Since the inclination angles must be high, this indicates that the accretion disc plays an important role in producing this type of the profile, but not the wind. The rareness of this type in the observation can be understood by the required high inclination angle (almost edge-on) in our models.

#### Type IV-B:

xxx describe this type xxxx

This type of the profiles is very similar to Type III-B, but the wind in this type of profile may be accelerating faster (a smaller  $\beta$  value) than that in Type III-B. In the models with the disc-wind, this type is seen at moderate to high inclinations ( $60^\circ \lesssim i \lesssim 80^\circ$ ) with relatively small value of the acceleration parameters ( $\beta \lesssim 0.5$ ).

#### Type IV-R:

xxx describe this type xxxx

This is the second least common type of the observed profiles (5 per cent) which shows the inverse P-Cyg profile shape. This can be understood since the magnetospheric accretion model of Hartmann et al. (1994) predicts that the redshifted absorption can occur at a limited range of inclination angle ( $i \simeq 50^\circ$ , but depends on the geometry of the magnetosphere) with which the hot continuum flux from the footprint of the magnetosphere is seen through relatively fast moving gas in the accretion stream. The wind component must be very weak. The mass-accretion rate should be much lower ( $\dot{M}_{\text{acc}} \sim 10^{-9} M_{\odot} \text{ yr}^{-1}$ ) than that of the models which produce Type I profiles since the flux in the broadening wings can not be too high to produce the inverse P-Cyg profile.

## 5.2 Inclination dependency of H $\alpha$ profiles

In the previous sections, we have considered the H $\alpha$  line formations in the disc wind which mimic the density distribution of the magneto-centrifugal launched jet numerical models (e.g. Krasnopolsky et al. 2003). The density in this model is more concentrated toward the equatorial plane in near field. In this section, we investigate the consistency of the line formation in the disc-wind model with the recent observation of Appenzeller et al. (2005) by concentrating on the inclination dependency of the EW of H $\alpha$ . Their study showed that the line equivalent width of CTTS increases as the inclination angle increases.

The right panel in Figure 13 shows the profiles computed with the disc-wind, magnetosphere hybrid model (section 4.2) at inclination angles  $i = 10^\circ, 55^\circ$  and  $80^\circ$ . The magnetospheric accretion component uses the parameters used as the reference model (Table 1). The figure shows that the absorption feature becomes stronger as the inclination increases, mainly because of the geometrical configuration. The optical depth becomes larger as the inclination angle increases since there is more material towards the equatorial plane. This tendency of the inclination dependency holds for the models with the wide ranges of  $\beta$  and  $T_{\text{wind}}$  values. As a result, the EW becomes smaller as the inclination angle increases: 41Å, 27Å, and 19Å for  $i = 10^\circ, 55^\circ$ , and  $80^\circ$  respectively. Clearly, this is not consistent with the trend seen in the observation of Appenzeller et al. (2005). Recall that a similar inclination dependency was found for the models with only magnetosphere (Figure 5).

We have also considered an alternative wind model which would produce the inclination dependency of the H $\alpha$  EW seen in the observation. In this model, the disc-wind is replaced by the stellar wind moving only in radial direction with the classical beta-velocity law (c.f. Castor & Lamers 1979) i.e.  $v_r(r) = v_{\infty}(1 - R_*/r)^{\beta}$  where  $v_{\infty}$  and  $R_*$  are the wind terminal velocity and the stellar radius respectively.  $\beta$  is the wind acceleration parameter similar to the one seen in the disc-wind model (c.f. equation 5). The wind emerges from the stellar surface, but restricted to be within  $\sim 30^\circ$  from the symmetry axis hence forming the cone-shaped regions both above and below the poles. The density is computed from assuming the constant mass-loss rate per unit area over the stellar surface, the mass-flux conservation, and using the beta velocity low above. The schematic of the model config-

**Table 6.** The summary model parameters for the profiles in Figure 12 and brief comments. The temperatures are in  $10^3$  K.  $\dot{M}_{\text{acc}}$  and  $\dot{M}_{\text{wind}}$  are in  $M_{\odot} \text{ yr}^{-1}$ .

Class	$i$	$\dot{M}_{\text{acc}}$	$T_{\text{max}}$	$\dot{M}_{\text{wind}}$	$T_{\text{wind}}$	$\beta$	Comment
I	55	$10^{-7}$	7.5	—	—	—	Accretion dominated possibly without the wind. Mid inclination.
II-B	55	$10^{-7}$	7.5	$10^{-8}$	8.0	1.0	Wind, disc and magnetosphere. Wide range of wind acceleration rate. Mid–high inclination
III-B	55	$10^{-7}$	7.5	$10^{-8}$	9.0	0.5	Wind, disc and magnetosphere. Fast–mid wind acceleration rate. Mid–high inclination
IV-B	55	$10^{-7}$	7.5	$10^{-8}$	9.0	0.2	Wind, disc and magnetosphere. Fast wind acceleration rate. Mid–high inclination
II-R	80	$10^{-7}$	7.5	$10^{-8}$	7.0	2.0	Wind, disc and magnetosphere. Slow wind acceleration rate. High inclination
III-R	85	$10^{-8}$	8.2	$10^{-9}$	6.0	1.0	Wind, disc and magnetosphere. Mid wind acceleration rate. Very high inclination
IV-R	55	$10^{-9}$	9.5	—	—	—	Accretion dominated. Low mass-accretion rate. Mid inclination.

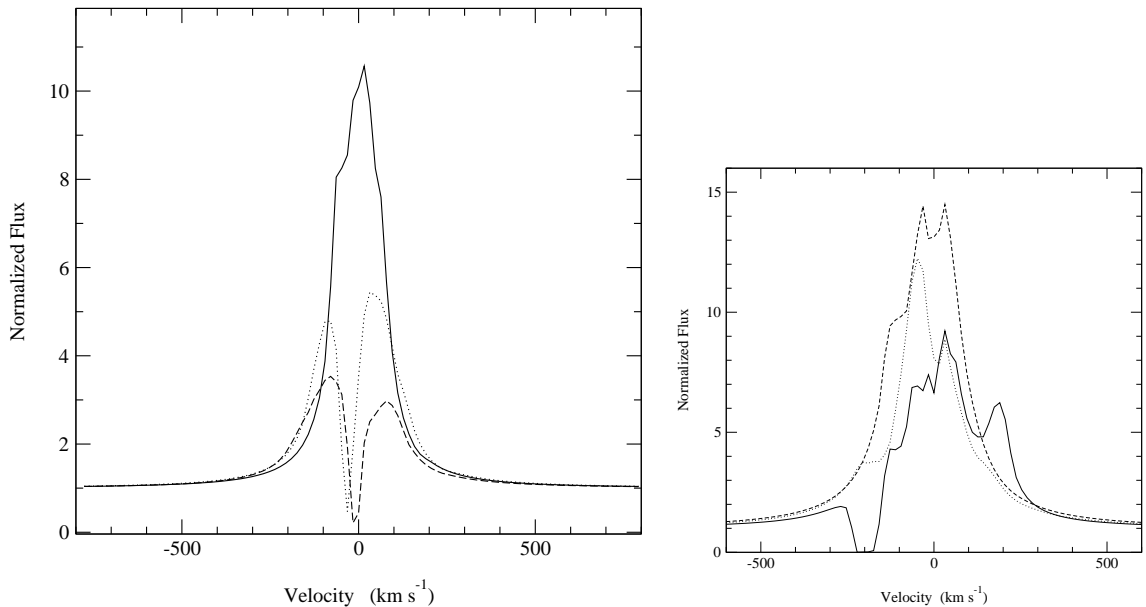


**Figure 13.** Dependency of the H $\alpha$  model profiles on the inclination angle. The profiles computed at  $i = 10^\circ$  (solid),  $55^\circ$  (dot) and  $80^\circ$  (dash) using (1) the disc-wind-magnetosphere hybrid model (left; c.f. section 4.2) and (2) the disc, stellar wind, magnetosphere hybrid model (right panel; c.f. Figure 14) are shown for a comparison. The parameters used for the magnetosphere are same for the both models, i.e.  $T_{\text{max}} = 7500$  K and  $\dot{M}_{\text{acc}} = 10^{-7} M_{\odot} \text{ yr}^{-1}$ . The isothermal wind temperature and the wind acceleration parameter used in (1) are  $T_{\text{wind}} = 7000$  K and  $\beta = 1.0$ , and those in (2) are  $T_{\text{wind}} = 9000$  K and  $\beta = 0.5$  respectively. All the other parameters are same as in sections 4.3 and 4.2. While the line equivalent width decreases as the inclination angle increases for the disc-wind model, it increases as the inclination angle increases for the stellar wind model. Only the latter agrees with the tendency seen in the observational study of Appenzeller et al. (2005) who showed that the H $\alpha$  line equivalent width of CTTS increases as the inclination angle increases.

uration is shown in Figure 14. Again, we assume the wind temperature ( $T_{\text{wind}}$ ) is isothermal for simplicity. This model configuration is motivated by the recent study by Matt & Pudritz (2005) who demonstrated the possibility that the stellar wind along the open magnetic field originated from the star can cause significant spin-down torque on the star, provided that mass-loss rate is high enough.

The right panel in Figure 13 shows the H $\alpha$  profiles computed using the alternative hybrid model at the same inclination angles used for the disc-wind-magnetosphere hybrid model. The wind acceleration parameter ( $\beta$ ) and the wind temperature ( $T_{\text{wind}}$ ) used here are 0.5 and 9000 K respectively. All the other parameters are same as in the disc-wind magnetosphere model. With this set of  $\beta$  and  $T_{\text{wind}}$ , the wind emission is comparable or a slightly greater than the emission from the magnetosphere. The profiles show rather complex absorption features because of the interaction of photons created in the wind with the magnetosphere. While the blue-shifted

absorption features are formed in the wind, the absorption features near the line centre and in the red wing (only for  $i = 10^\circ$ ) are caused by the wind emission by the magnetosphere which has a rather complex flow geometry. Because of the geometry of the wind, the P-Cyg absorption feature weakens as the inclination increases. The optical depth of the wind is much higher in the polar direction compared to that at higher inclination. For the same reason, the EW of the line increases as the inclination increase as clearly seen in the figure. Specifically their values are 49Å, 60Å, and 84Å for  $i = 10^\circ$ ,  $55^\circ$ , and  $80^\circ$  respectively. This tendency of the inclination dependency holds for the models with this wind models for wide ranges of  $\beta$  and  $T_{\text{wind}}$  as long as the emission from the wind is comparable to that of the magnetosphere.

The distinct difference in the density dependency on the polar angles in two different wind models should be apparent in the inclination angle dependency on the observed line profiles. For example, one possible way to distinguish the two different wind models

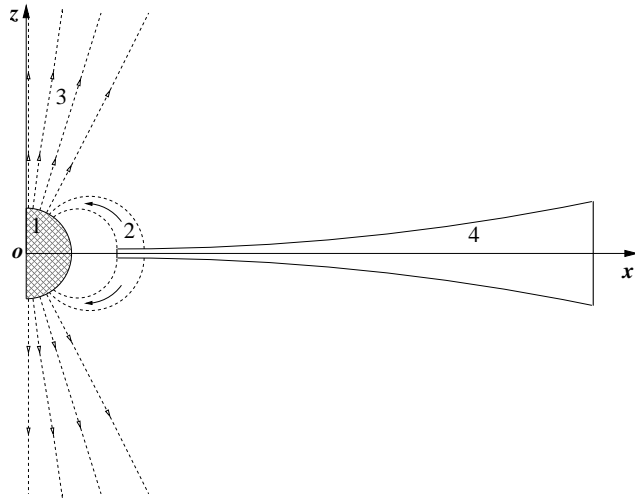


**Figure 14.** The alternative hybrid model. The model replaces the disc-wind in the previous hybrid model with the stellar wind. The wind launching from the stellar surface is limited within the cones with the opening angle  $\sim 30^\circ$  to avoid the wind from overlapping with the magnetosphere. The system consists of four components: (1) the continuum source located at the origin ( $o$ ) of the cartesian coordinates ( $x, y, z$ ) – the  $y$ -axis is into the paper, (2) the magnetospheric accretion flow, (3) the stellar wind outflow, and (4) the accretion disc. The density distribution is symmetric around the  $z$ -axis.

is to examine the profile shape of a CTTS which is known to be viewed at pole-on. If the profile contains a prominent blue-shifted absorption component (e.g. Type IV-B), the system is more likely to be associated with the ‘bipolar’ stellar wind type of outflow (but not with the disc-wind type of outflow). In reality, two types of the winds (bipolar stellar wind and disc wind) may co-exists similar to that seen in e.g. Drew, Proga, & Stone (1998) and Matt & Pudritz (2005). In these models, the fast stellar wind is present in the polar directions, and at the same time the slower disc wind is present near the equatorial plane.

The extensive parameter studies of the simple stellar wind model presented in this section have not been performed. The models presented here are for a demonstrative purpose, and the further investigation is necessary before the models are applied to a real system, perhaps, by combining our radiative transfer model with the results from MHD ‘stellar’ wind calculations.

In this analysis, we found only the models with the bipolar stellar wind agree with the trend seen in their observation. Although the uncertainty in the inclination angles of the observed object might be large, a larger sample in addition to that of Appenzeller et al. (2005) for further investigation of the inclination dependency on the line profile will be extremely useful for determining the wind configuration of CTTS.

## 6 CONCLUSIONS

We have presented the disc-wind-magnetosphere hybrid radiative transfer models for classical T Tauri stars, and detailed studies of the H $\alpha$  formation from their complex to circumstellar environment. We found that hybrid model can reproduce the wide variety of profile seen in observations (Figures 3, 6, 9 and 12). Especially, the blue-shifted wind absorption feature very commonly seen in the H $\alpha$  profile of CTTS were well understood by this model. This

was not possible in the magnetospherical accretion only model presented in earlier works (e.g. Muzerolle et al. 2001).

The profiles computed with the hybrid model showed that the wind emission contribution becomes significantly larger than that from the magnetosphere (Figure 9 and Table 5). Henceforth, a large H $\alpha$  equivalent width does not necessary indicate a large mass-accretion rate, but it could be caused by the mass-loss by the wind outflow.

Using the model results, we examined the H $\alpha$  spectroscopic classification proposed by Reipurth et al. (1996), and discussed the basic physical conditions that reproduce the profiles in each classified type (section 5.1). Using the different combinations of the inclination ( $i$ ), the mass-loss to mass-accretion rate ratio ( $\mu$ ) and the wind acceleration rate ( $\beta$ ), our radiative transfer model was able to produce all 7 classes of profiles defined in Reipurth et al. (1996).

The value of  $\mu$ , 0.1, suggested by both MHD calculations and observations (c.f. Königl & Pudritz 2000) is consistent with the disc-wind-magnetosphere models presented here. We found that the hybrid models with  $0.05 < \mu < 0.2$  are also consistent with the type of the profiles seen in the observations (e.g. Reipurth et al. 1996).

Unfortunately, the dependency of the line equivalent width on the inclination angle predicted by the disc-wind-magnetosphere hybrid model does not agree with the trend seen in the observation of Appenzeller et al. (2005); however, their results are based on a small number of objects (12). We have also considered an alternative hybrid model in which the disc-wind is replaced by the narrow cone-shaped stellar wind, and found that the alternative wind hybrid model can reasonably reproduces the line equivalent width dependency on the inclination seen in the observation (Figure 13).

Similar model configurations used here may be also applicable to Herbig Ae/Be and brown dwarfs since their H $\alpha$  observations also exhibit evidence of the outflow and inflow (e.g. Finkenzeller & Mundt (1984); Muzerolle et al. 2005), but no model has been developed to explain the phenomenon. Further investigation on the possibility of applying our model to these objects are needed.

Future work should include the followings: (1) Improving the wind models. The parametrisation of the wind density structure should be changed to follow more closely that of MHD simulations. The wind temperature structure should be calculated self-consistently (c.f. Hartmann et al. 1994; Martin 1996). (2) Computing the line profiles using the density structure from MHD directly. Check the consistency, and give feedback to the MHD models which are needed to be tested against observational data. (3) Spectropolarimetric study to explore the geometry and the rotation of the disc (e.g. Vink et al. 2005). (4) Modelling of the extended H $\alpha$  and spectro-astrometric observations (c.f. Takami et al. 2003; Appenzeller et al. 2005). (5) Line variability study using a 3D radiative transfer model (e.g. Symington et al. 2005a; Kurosawa et al. 2005) to probe the geometrical structure.

## ACKNOWLEDGEMENTS

Authors thank Jorick Vink for providing us the H $\alpha$  data of T Tau. This work is supported by PPARC standard grant PPA/G/S/2001/00081.

## References

- Alencar S. H. P., Basri G., 2000, AJ, 119, 1881

- Alencar S. H. P., Basri G., Hartmann L., Calvet N., 2005, A&A, 440, 595
- Anders E., Grevesse N., 1989, *geochim. cosmochim. acta*, 53, 197
- Appenzeller I., Bertout C., Stahl O., 2005, A&A, 434, 1005
- Appenzeller I., Mundt R., 1989, A&AR, 1, 291
- Bertout C., Basri G., Bouvier J., 1988, ApJ, 330, 350
- Blandford R. D., Payne D. G., 1982, MNRAS, 199, 883
- Burrows C. J., Stapelfeldt K. R., Watson A. M., Krist J. E., Ballester G. E., Clarke J. T., Crisp D., Gallagher J. S., Griffiths R. E., Hester J. J., Hoessel J. G., Holtzman J. A., Mould J. R., Scowen P. A., Trauger J. T., Westphal J. A., 1996, ApJ, 473, 437
- Camenzind M., 1990, *Reviews of Modern Astronomy*, 3, 234
- Castor J. I., Abbott D. C., Klein R. I., 1975, ApJ, 195, 157
- Castor J. I., Lamers H. J. G. L. M., 1979, ApJS, 39, 481
- Chiang E. I., Goldreich P., 1997, ApJ, 490, 368
- Collier Cameron A., Campbell C. G., 1993, A&A, 274, 309
- Draine B. T., Lee H. M., 1984, ApJ, 285, 89
- Drew J. E., Proga D., Stone J. M., 1998, MNRAS, 296, L6
- Edwards S., Cabrit S., Strom S. E., Heyer I., Strom K. M., Anderson E., 1987, ApJ, 321, 473
- Edwards S., Hartigan P., Ghandour L., Andrulis C., 1994, AJ, 108, 1056
- Finkenzeller U., Mundt R., 1984, A&AS, 55, 109
- Frank J., King A., Raine D. J., 2002, *Accretion Power in Astrophysics*, 3rd edn. Cambridge Univ. Press, Cambridge, p. 398
- Ghosh P., Pethick C. J., Lamb F. K., 1977, ApJ, 217, 578
- Grevesse N., Noels A., 1993, in *Origin and Evolution of the Elements*, N. P. E. V.-F., M. C., eds., Cambridge Univ. Press, Cambridge, p. 15
- Gullbring E., Hartmann L., Briceno C., Calvet N., 1998, ApJ, 492, 323
- Hanner M., 1988, in NASA Conf. Pub. 3004, 22, Vol. 3004, p. 22
- Harries T. J., 2000, MNRAS, 315, 722
- Hartigan P., Edwards S., Ghandour L., 1995, ApJ, 452, 736
- Hartmann L., Avrett E., Edwards S., 1982, ApJ, 261, 279
- Hartmann L., Hewett R., Calvet N., 1994, ApJ, 426, 669
- Herbig G. H., 1962, *Advances in Astronomy and Astrophysics*, 1, 47
- Herbig G. H., Bell K. R., 1988, Catalog of emission line stars of the orion population, Vol. 3. Lick Observatory Bulletin, Santa Cruz: Lick Observatory
- Hillier D. J., 1991, A&A, 247, 455
- Johns-Krull C. M., Valenti J. A., Hatzes A. P., Kanaan A., 1999, ApJ, 510, L41
- Kenyon S. J., Hartmann L., 1987, ApJ, 323, 714
- Kenyon S. J., Hartmann L., Hewett R., Carrasco Cruz-Gonzalez I., Recillas E., Salas L., Serrano A., Strom K. M., Strom S. E., Newton G., 1994, AJ, 107, 2153
- Kim S., Martin P. G., Hendry P. D., 1994, ApJ, 422, 164
- Klein R. I., Castor J. I., 1978, ApJ, 220, 902
- Knigge C., Woods J. A., Drew E., 1995, MNRAS, 273, 225
- Königl A., 1991, ApJ, 370, L39
- Königl A., Pudritz R. E., 2000, *Protostars and Planets IV*, 759
- Krasnopolsky R., Li Z.-Y., Blandford R. D., 2003, ApJ, 595, 631
- Kuhi L. V., 1964, ApJ, 140, 1409
- Kurosawa R., Harries T. J., Bate M. R., Symington N. H., 2004, MNRAS, 351, 1134
- Kurosawa R., Harries T. J., Symington N. H., 2005, MNRAS, 358, 671
- Kurucz R. L., 1979, ApJS, 40, 1
- Long K. S., Knigge C., 2002, ApJ, 579, 725
- Luttermoser D. G., Johnson H. R., 1992, ApJ, 388, 579
- Martin S. C., 1996, ApJ, 470, 537
- Mathis J. S., Rumpl W., Nordsieck K. H., 1977, ApJ, 217, 425
- Matt S., Pudritz R. E., 2005, ApJ, 632, L135
- Mihalas D., 1978, *Stellar atmospheres*, 2nd edn. W. H. Freeman and Co., San Francisco
- Muzerolle J., Calvet N., Hartmann L., 2001, ApJ, 550, 944
- Muzerolle J., Luhman K. L., Briceño C., Hartmann L., Calvet N., 2005, ApJ, 625, 906
- Ouyed R., Pudritz R. E., 1997, ApJ, 482, 712
- Pudritz R. E., Banerjee R., 2005, in IAU Symposium, pp. 163–173
- Ray T. P., Mundt R., Dyson J. E., Falle S. A. E. G., Raga A. C., 1996, ApJ, 468, L103
- Reipurth B., Pedrosa A., Lago M. T. V. T., 1996, A&AS, 120, 229
- Rybicki G. B., Hummer D. G., 1978, ApJ, 219, 654
- Shakura N. I., Sunyaev R. A., 1973, A&A, 24, 337
- Shang H., Glassgold A. E., Shu F. H., Lizano S., 2002, ApJ, 564, 853
- Shu F. H., Najita J., Ostriker E., Wilkin F., Ruden S., Lizano S., 1994, ApJ, 429, 781
- Symington N. H., Harries T. J., Kurosawa R., 2005a, MNRAS, 356, 1489
- Symington N. H., Harries T. J., Kurosawa R., Naylor T., 2005b, MNRAS, 358, 977
- Takami M., Bailey J., Chrysostomou A., 2003, A&A, 397, 675
- Uchida Y., Shibata K., 1985, PASJ, 37, 515
- Ustyugova G. V., Koldoba A. V., Romanova M. M., Chechetkin V. M., Lovelace R. V. E., 1995, ApJ, 439, L39
- Vernazza J. E., Avrett E. H., Loeser R., 1973, ApJ, 184, 605
- Vink J. S., Drew J. E., Harries T. J., Oudmaijer R. D., Unruh Y., 2005, MNRAS, 359, 1049
- White R. J., Basri G., 2003, ApJ, 582, 1109
- Whitney B. A., Wood K., Bjorkman J. E., Wolff M. J., 2003, ApJ, 591, 1049
- Wood K., Wolff M. J., Bjorkman J. E., Whitney B., 2002, ApJ, 564, 887

#### APPENDIX A: H $\alpha$ ATLAS OF THE DISC-WIND-MAGNETOSPHERE HYBRID MODEL

Here we present xxxxxxxxxxxxxxxx.

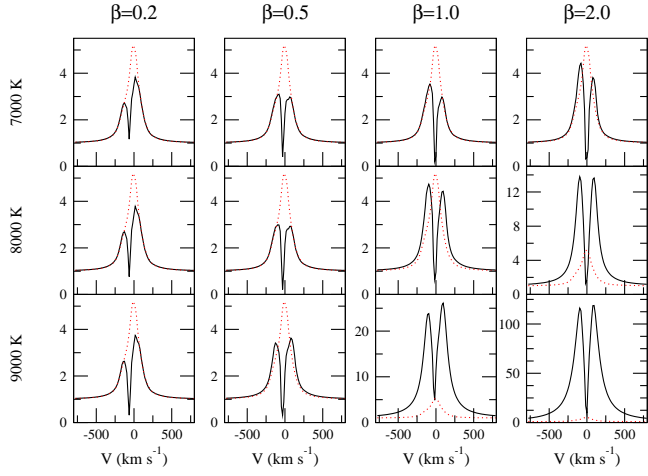
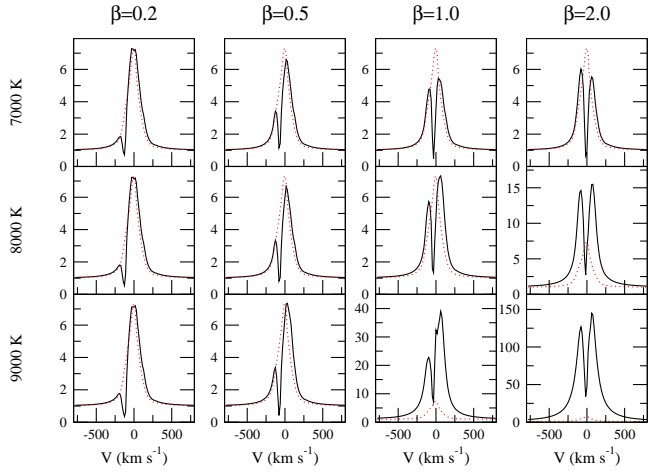
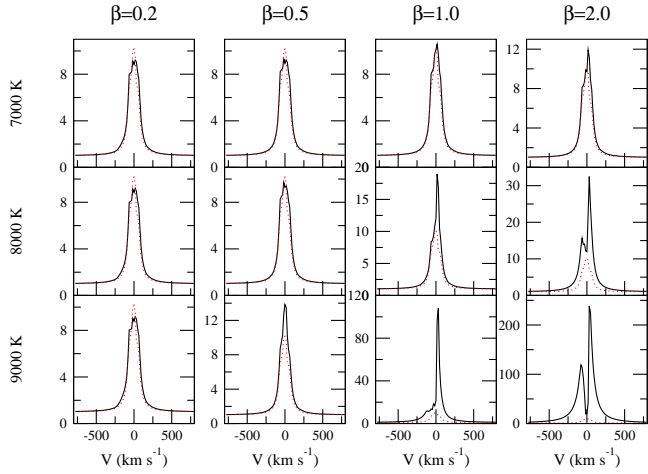


**Figure A1.** The H $\alpha$  atlas of the disc-wind-magnetosphere hybrid model with  $M_{\text{acc}} = 10^{-7} M_{\odot} \text{ yr}^{-1}$  and  $M_{\text{wind}} = 10^{-6} M_{\odot} \text{ yr}^{-1}$ .

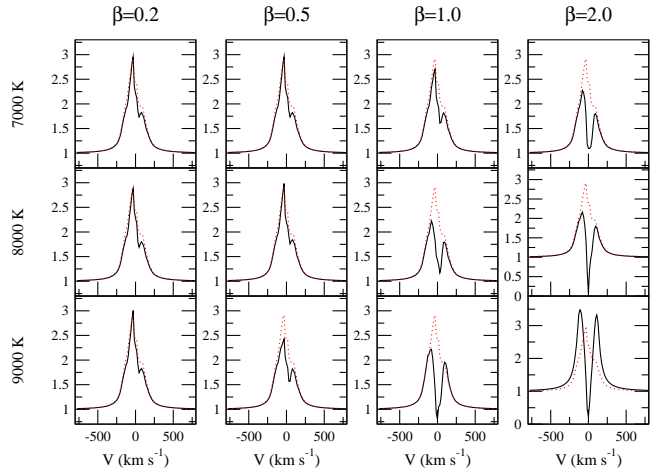
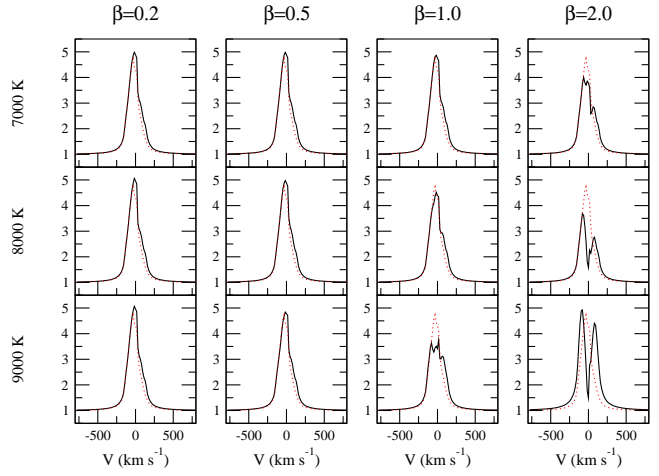
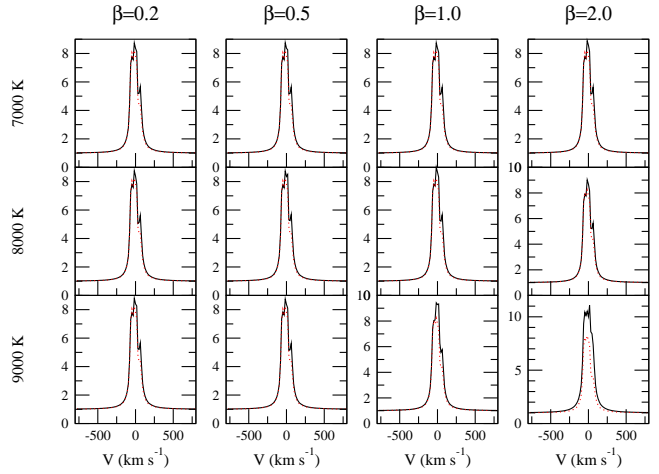


**Figure A2.** The H $\alpha$  atlas of the disc-wind-magnetosphere hybrid model with  $M_{\text{acc}} = 10^{-8} M_{\odot} \text{ yr}^{-1}$  and  $M_{\text{wind}} = 10^{-7} M_{\odot} \text{ yr}^{-1}$ .

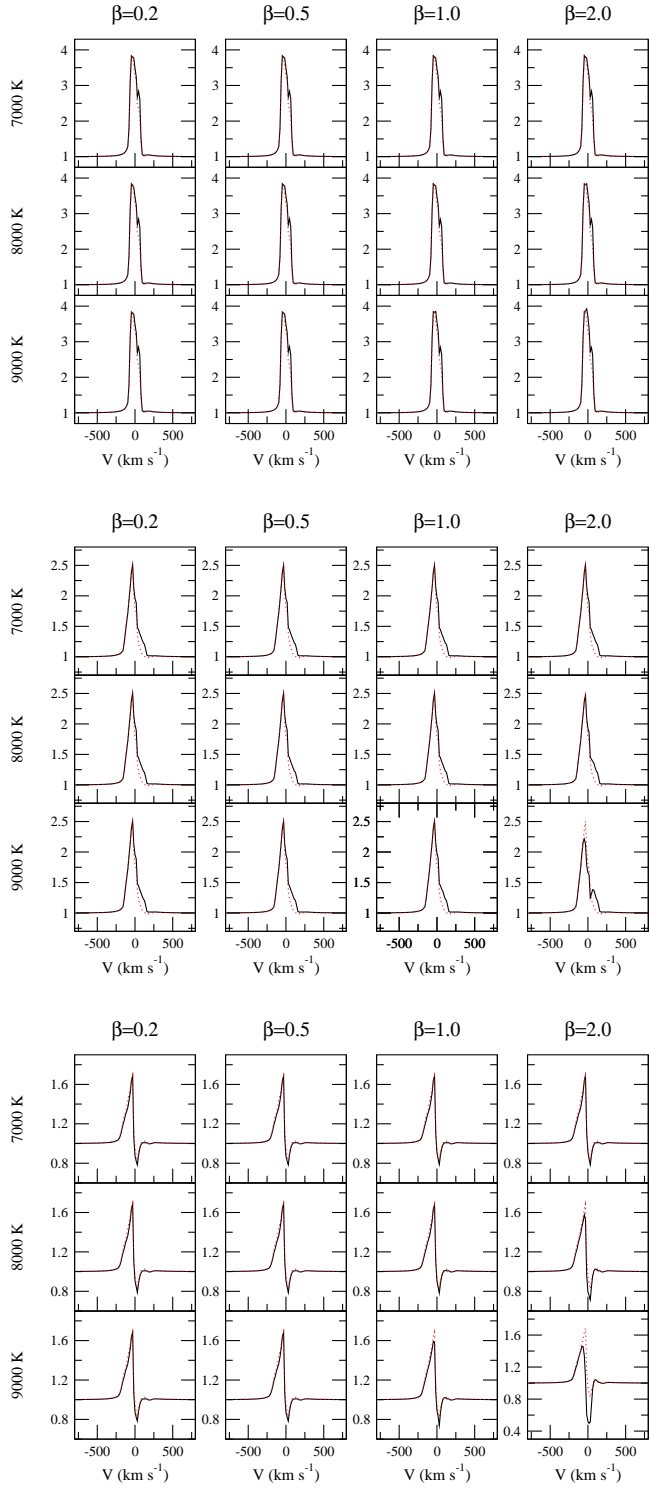


**Figure A3.** The H $\alpha$  atlas of the disc-wind-magnetosphere hybrid model with  $M_{\text{acc}} = 10^{-9} M_{\odot} \text{ yr}^{-1}$  and  $M_{\text{wind}} = 10^{-10} M_{\odot} \text{ yr}^{-1}$ .